UNIVERSITY OF OKLAHOMA

GRADUATE COLLEGE

FORWARD SEISMIC MODEL OF PERMIAN GUADALUPIAN SHELF-TO-BASIN

SEDIMENTATION THROUGH NOVEL INTEGRATION OF LIDAR AND

SCHMIDT HAMMER, MCKITTRICK CANYON, WEST TEXAS

A THESIS

SUBMITTED TO THE GRADUATE FACULTY

in partial fulfillment of the requirements for the

Degree of

MASTER OF SCIENCE

By

ZHUOBO WANG
Norman, Oklahoma
2018

FORWARD SEISMIC MODEL OF PERMIAN GUADALUPIAN SHELF-TO-BASIN
SEDIMENTATION THROUGH NOVEL INTEGRATION OF LIDAR AND
SCHMIDT HAMMER, MCKITTRICK CANYON, WEST TEXAS

A THESIS APPROVED FOR THE
CONOCOPHILLIPS SCHOOL OF GEOLOGY AND GEOPHYSICS

BY

_____
Dr. John D. Pigott, Chair

_____
Dr. Kurt J. Marfurt

_____
Dr. Kulwadee L. Pigott

ACKNOWLEDGEMENTS

Table of Contents

LIST OF TABLES

LIST OF FIGURES

ABSTRACT

As a result of the challenges occurring with the subsurface seismic interpretation of images of the complicated depositional systems of the Guadalupian of the Permian Basin, forward seismic model is built to guide the subsurface interpretation of a steep-rimmed shelf margin setting and toe-of-slope profile of a prograding reef-rimmed shelf and clinoform exposed on the north wall of McKittrick Canyon of Guadalupe Mountains. This study integrates Light Detection and Ranging (LiDAR), Schmidt hammer and density measurements to craft a seismic analogue.

The stratigraphic frame is established using high-resolution point cloud scanned by RIEGL VZ-400i, containing upper Yates Formation and lower Tansill Formation at the shelf and their equivalent members of Bell Canyon Formation at slope-to-basin section. Three high frequency Late Guadalupian sequences (HFSs) (Tinker, 1998), including Y5, Y6 and T1 are defined in the frame. Slope equivalents of these HFSs are characterized by HST carbonate members with underlying LST bypass siliciclastics, which correlate to the Y5, Y6 and T1 with the McComb Limestone, the McKittrick Canyon Limestone and the Lamar Limestone, respectively. The indirect estimation of P-wave velocity is completed through an empirical relationship between P-wave velocity and Schmidt hammer rebound number (R) and, subsequently, relationship between R and velocity ratio Q (velocity ratio: geomechanical ratio of impact velocity to rebound velocity) which is collected by electric Schmidt hammer applied in this study. Data analysis reveals the heterogeneity of acoustic impedance of each stratum from proximal to distal slope. Deposit-position based trend of impedance variation is

discovered by fitting impedance against normalized along-slope distance, which contributes to the impedance model establishment.

A vertical incidence synthetic seismogram is computed upon the geologic model built with LiDAR assisted stratigraphic frame and situ petrophysical information. A zero-phase wavelet of 250 Hz Nyquist are used in the convolution with the reflection coefficient matrix to simulate a seismic profile at study area under ideal conditions. Two additional models are simulated by wavelets of lower band width (125Hz Nyquist) with and without random noise added to establish a comparable profile to general quality seismic data. The first two synthetic seismic profiles show comparable stratigraphic architectures to stratigraphy interpretation on LiDAR while the model simulated by wavelet with band pass of 2, 8, 62.5, 80 Hz exhibits poor resolution and model-induced artifacts.

This investigation shows the potential value of extrapolating an outcrop-based forward seismic model of complicated carbonate in order to provide insight into the subsurface.

CHAPTER 1: INTRODUCTION

Reflection seismology is widely utilized in hydrocarbon exploration to help investigate subsurface geology features of a potential petroleum target area. Among the techniques of seismic interpretation, the employment of seismic stratigraphic analysis, a step to extract stratigraphic information, predict reservoir, seal and source rock geometries, and therefore, to approach a better understanding of subsurface petroleum system through geological time scale. Although many studies of carbonate slope depositional systems have been published (Saller et al., 1999; Tinker, 1996; Ward et al.,1996), difficulties of interpreting the seismic stratigraphy at the shelf margin through slope to basin remain owing to complicated depositional systems and poorly-understood seismic responses (Palaz and Marfurt, 1997). Therefore, an outcrop-constrained forward seismic modeling technique could potentially be a powerful tool for a stratigraphic interpretation of a referred analogue. This work proposes such an approach with a novel integration of LiDAR with the Schmidt hammer in order to craft just such an outcrop-constrained forward seismic model.

This study integrates the Light Detection and Ranging (LiDAR) instrument, the Schmidt hammer and density measurements for providing petrophysical insight into the Middle to Late Guadalupian slope profile at McKittrick Canyon, based on the stratigraphic frame and impedance model, the synthetic seismic model presents complicated architectural elements with seismic response at a subseismic scale. This work not only conducts the first outcrop based seismic model of McKittrick Canyon, but also is the first to apply LiDAR and Schmidt hammer together to assist field work.

Study Location

Located at west Texas, the Delaware basin is bounded by the Northwest Shelf at Guadalupe Mountains (Figure 1). Among several major dip-oriented canyons of the Guadalupe Mountains, the transect of prograding reef-rimmed shelf and clinoform deposition of Late Guadalupain can be observed on the south and north walls of McKittrick Canyon (Figure 2) (King, 1948; Newell et al., 1953; Hayes, 1964).
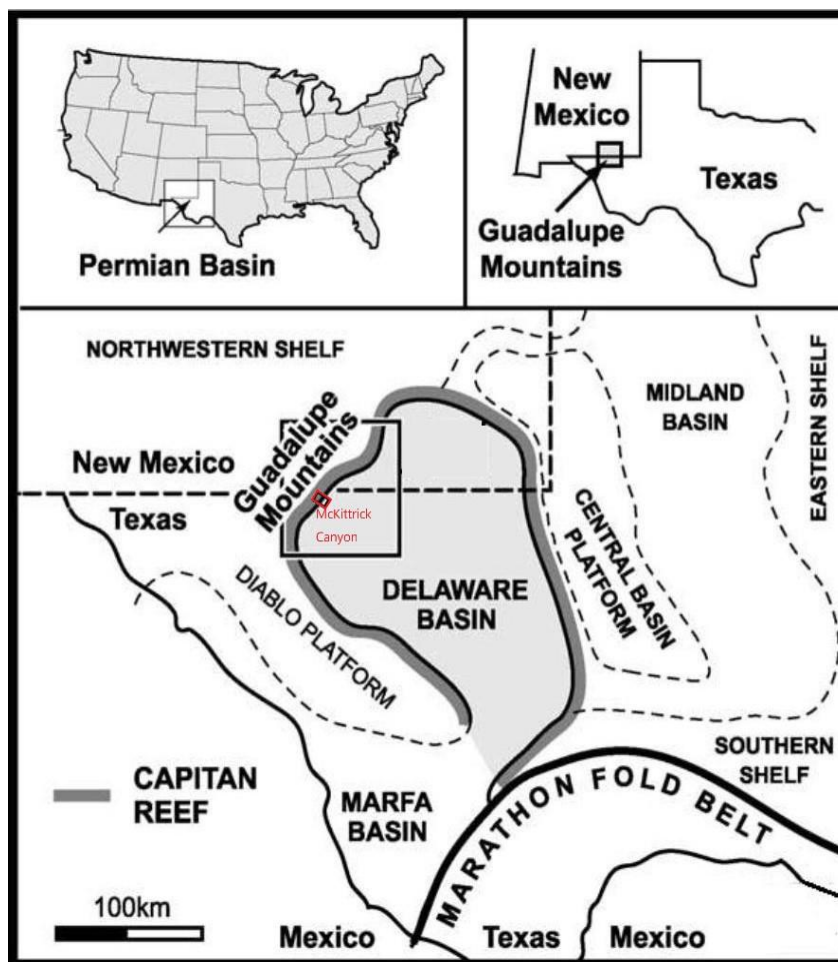
Figure 1: Simplified map of Geologic Provinces within the greater Permain Basin.
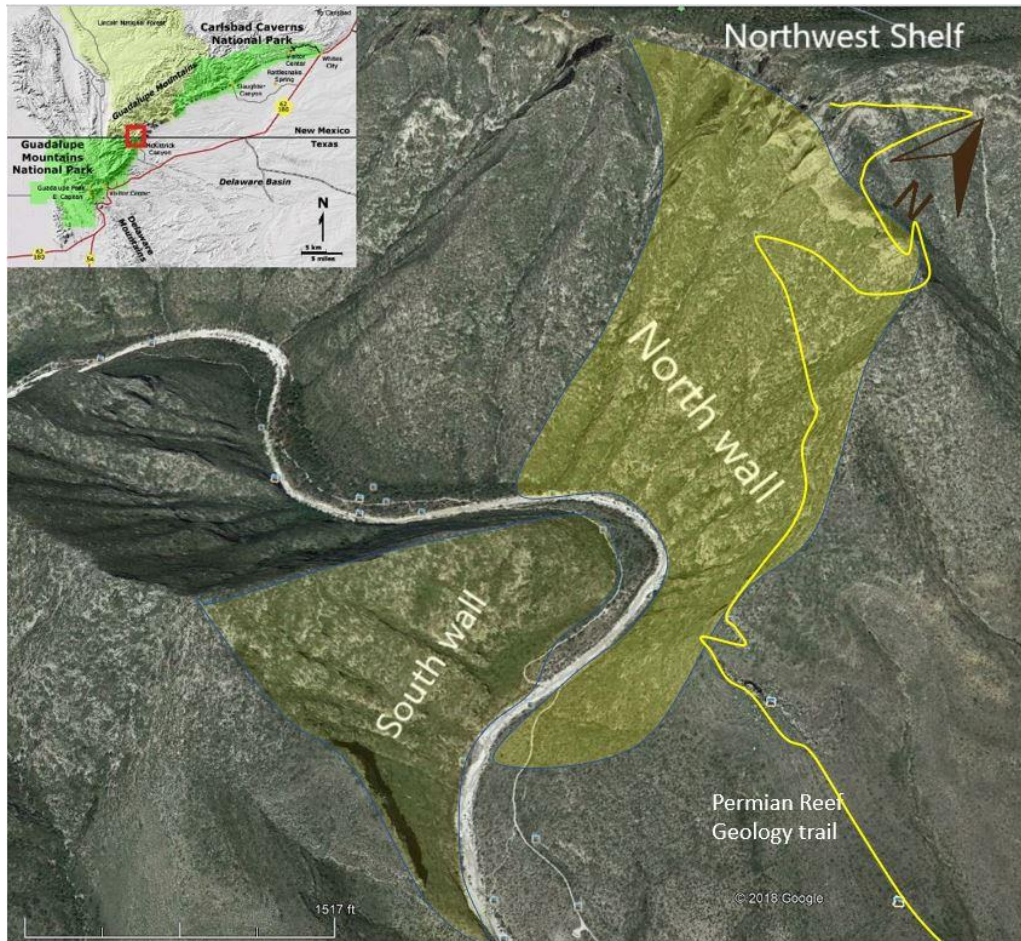
Figure 2: McKittrick Canyon 3D view from Google Earth. Study area is in yellow shadow, and Permian Reef Geology trail is marked by yellow solid line.

Problem definition

Shelf-to-basin stratigraphic interpretation on subsurface seismic profiles is challenging owing to complicated depositional systems caused by frequent sea level change, especially on a steep reef-rimmed siliciclastic-carbonate mixing slope profile (Garrett and Pigott, 2015, Garrett et al., 2016). Remaining uncertainties exist in key boundary tracing, clinoform stacking pattern description and sequence stratigraphy from well-bedded shelf and shelf crest strata, through reef and fore-reef complex, slope clinoform, into bedded toe-of-slope and basinal units. A high resolution forward seismic

model of shelf-to-basin is needed to guide seismic interpretation of analogues in the subsurface.

The objectives are to 1) conduct Light Detection and Ranging(LiDAR) scanning for the outcrop exposed at the mouth of McKittrick Canyon; 2) build a stratigraphic model of shelf-to-basin deposition on LiDAR point cloud data; 3) collect velocity ratio Q of Schmidt Hammer, contributing to estimation of P-wave velocity on exposed outcrop for each deposit unit; 4) conduct an accurate impedance model from a massive data set upon a stratigraphic frame; 5) generate a forward seismic model by convolution of input wavelets of contemporary industry and supraindustry frequency band width with defined stratigraphic impedance model; 6) and describe the observed geometric results of the synthetic model.

These results will potentially contribute to the accurate stratigraphic interpretation of seismic data at shelf, slope and toe-of-slope basinal area under similar conditions in the petroleum industry.

Previous work

Forward seismic modeling has greatly developed in the last three decades from convolution based 1-D methods, to finite-difference (FD) and finite-element (FE) modeling of 2-D and 3-D models. With increasing demand of more accurate subsurface interpretation of seismic in complicated exploration areas, geophysical methods in stratigraphically complex areas can be improved as combining stratigraphic architecture and lithologic distributions observed in outcrop to petrophysical properties obtained

from core measurements, density, and velocity logs in order to provide a more accurate seismic interpretation. A short-cut to cores is to simple utilize outcrop data.

One of the first examples comparing synthetic seismic data with real seismic is a model built to study the genesis of the depositional geometries and accompanying facies of the Permain strata in the Guadalupe Mountain by Sarg (1987) who built a one-dimensional borehole seismic trace and two-dimensional forward model in this study area based upon data from wells, which only included basic structure-stratigraphic schemes. Following Sarg's model of a large-scale carbonate basin profile was Biddle et al. (1992) who modeled the progradational carbonate platform at Picco Vallandro which assigned the acoustic measurements from core plugs to each depositional environment (Biddle et al., 1992).

Utilizing the increased detail potentially provided in outcrop, Stafleu and Sonnenfeld (1994) conducted a forward seismic model of the Permain San Andres Formation in Last Chance Canyon which is a mixed siliciclastic-carbonate shelf-margin depositional system. Two models were built based on limited velocity data measured from core plugs of dominant lithofacies: one had contract at bedding planes and the other had at facies boundaries. They compared both models with a real seismic line located 50 km northwest of Last Chance Canyon acquired by Exxon, which indicated that the importance of facies changes.

Sullivan et al. (2000) have seismically forward modelled the Lower Permian Skoorstennberg Formation in the Tanqua Karoo Basin of South Africa and the Lower Carboniferous Ross Formation of the Clare Basin in western Ireland and compared the seismic characteristics of these to the Diana field in the western Gulf of Mexico.

To fulfill the requirement of exploration in different geological complexes, research on seismic modeling of specific depositional architectures were published in the past decade. Schwab et al. (2007) built a resultant synthetic seismic model based upon constant deterministic petrophysical properties with a binary sand-shale scheme to compare one seismic line from offset-stacked channels from the Elazig Basin (Turkey). Bakke et al. (2008) approached the seismic modeling of a turbidite system by using interpolated petrophysical properties from a well in Dalia field Spain, which was compared with subsurface seismic data of a Miocene turbidite complex of offshore Angola.

Gartner et al. (2001) built a synthetic seismic model of an Early Cretaceous slope of a carbonate platform with the aid of photo mosaics with an impedance model based upon velocity, density and porosity from spot samples. Falivenen et al. (2010) proposed a seismic model for the Eocene Ainsa Turbidite system, based on an outcrop-derived three-dimensional facies model. Janson and Fomel (2011) proposed an outcrop-based 3-D geocellular model to help the interpretation of steep slope carbonate deposition from Lower Permian deep-water carbonate gravity flow. While the results of these studies approach increasingly refined structural continuity of stratal reflectors, without an accompanying petrophysical samplings resolution, the models are limited in their ability to resolve stratigraphic complexities which after occuring at smaller scales than structural variations.

CHAPTER 2: GEOLOGICAL BACKGROUND

Tectonics

Originating as the Tobosa Basin, the Delaware Basin experienced periodic tectonism-active events from Early Paleozoic to Early Cenozoic (Williams, 2013). As the result of cooling of underlying rifted crust and mantle early in the Ordovician, the subsidence created a flattened coastal plain, defined as the Tobosa Basin (Galley, 1958), where sedimentation occurred and continued under a period of tectonic quiescence (Adams, 1965). In the middle of the Ordovician when the crustal warping ended, the Tobosa Basin developed into a 350-mile-wide basin which was bounded on the east by the Texas arch and the west by the Diablo arch (Adams, 1965).

Followed by Marathon-Ouachita orogeny, the tectonic quiescence time ended in Middle Mississippian when the Tobosa Basin was subjected to intense deformation caused by the collision between Laurasia with Gondwana. Under the southwest-to-northeast compression of the Ouichita-Marathon fold belt, the Tobosa basin was divided into two separate sub-basins, the Midland Basin and Delaware Basin, by the uplifted Central Platform, resulting the generation of Diablo Platform, Northwest Shelf and Eastern Shelf in the meantime (Hoark, 1985; Yang and Dorobek, 1995; Miall, 2008) but with the complication of lithospheric flexure (Pigott, 2016). From the middle to late Pennsylvanian, structural activity increased throughout the region due to the Variscan Orogeny, causing dramatically uplifting of Central Platform and more subsidence of Delaware Basin (Hills, 1984; Yang and Dorobek, 1995, Williams, 2013).

The tectonism of the Delaware Basin ceased after sporadic tectonic activities led by the final pulses of the Marathon orogeny in the Early Permain (Hills, 1984). Eventually, the slight movement along the zone of weakness on the east of Delaware Basin induced the subsidence of the basin floor, a 1000-foot falling below the surrounding carbonate shelves (Hills, 1984). The Delaware Basin accumulated massive sedimentation in tectonic stability throughout from Wolfcampian to Ochoan when the basin was filled with Castile evaporates.

Following Permo-Triassic burial, the compresional regime associated with the Laramide Orogeny partially exhumed the western side of the Guadalupe Mountains. Later, during extension of the Basin and Range Province in the Oligocene-Pliocene, the Northwest Shelf and Capitan Reef complex were partially exhumed along the Capitan Reef Escarpment, which represent the most eastern expression of NNW – SSE oriented Basin and Range high-angle normal faults (Hayes, 1964; Garber et al 1989).

The tectonic history of Delaware Basin stated above is also revealed by basin modeling, summarizing four episodes of tectonism which corresponds major tectonic activities mentioned above : 1) A Tobasa Rifting Phase (488-320 Ma), 2) A Permian Basin Phase (320-250 Ma), 3) A Stable Platform Phase (250-80 Ma), and 4) A Cenozoic Tectonic Uplift Phase (70-0 Ma) (Lew et al., 2013, Micheal et al., 2014, Pigott et al., 2014, Pigott et al., 2015, Pigott et al., 2016).

Stratigraphy

The exhumed Guadalupe Mountains, as the result of Early Cenozoic tectonic activity as stated above, exposed sedimentation which accumulated from the Middle to

Late Guadalupian, representing the complete system which includes the sequences of shelf, carbonate-rimmed shelf edge, slope and basin (Ward et al., 1986). Stratigraphically, the outcrop exposure in the McKittrick Canyon constitute the Capitan Depositional System, representing the Capitan Formation, the stratigraphic age equivalents on the shelf (Seven Rivers, Yates and Tansill formations), and the equivalents in the basin, known as the Bell Canyon Formation (Figure 3) (Newell et al., 1953; Saller et al., 1999).

The Capitan Formation (Figure 3) is comprised of the massive Capitan Reef with fore-slope reef talus complex which has 100-150 m of massive reef facies and 500-600 m for the total thickness (King, 1948). Characterized by thick carbonate intervals alternating with siliciclastic, the Seven Rivers Formation is bounded at its base by the Shattuck Sandstone member and at its top by the Yates Formation (Tait et al., 1962). The Yates Formation represents a mixed siliciclastic-carbonate evaporite shelf system which passes into the Capitan Formation (Ward, et al., 1986). Similar to the Yates Formation, the Tansill Formation is characterized by carbonate-evaporite shelf system while there is no siliciclastic dominated interval deposit. As the basin equivalent to Capitan reef complex, the Bell Canyon accumulated massive siliciclastic interbedded with distinctive carbonate members which comprise the toe-of-slope and proximal basin floor equivalent (Bosellini, 1984).
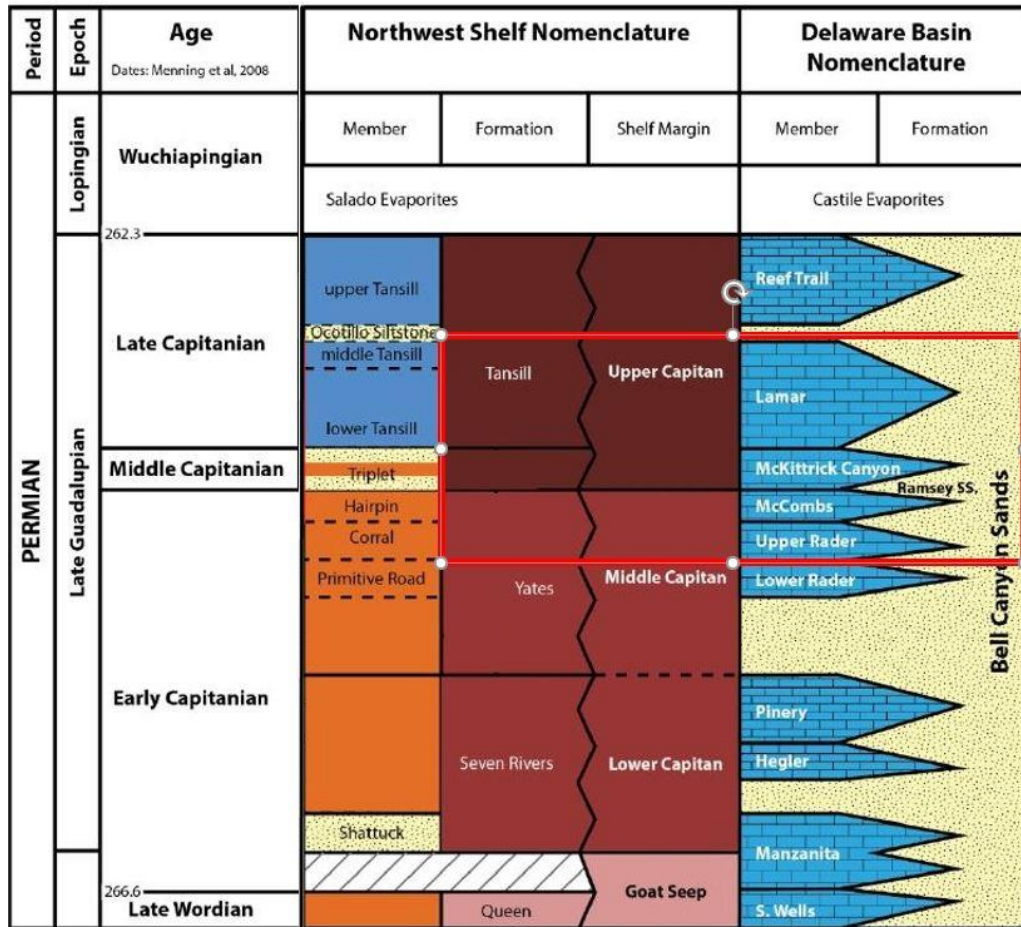
Figure 3: Detailed Late Gaudalupian rock-stratigraphic framework of the Delaware Mountain Group. Stratigraphy units developed on the north wall of McKittrick Canyon are boxed in red rectangular. Modified from Rush and Kerans (2010) and Kerans et al. (2011)

Sequence Stratigraphy

A global climatic transition, from Carboniferous icehouse to Mesozoic greenhouse conditions, is well expressed in the stratigraphic record of the Late Permian deposit profile where cyclicity dominates the shelf-to-basin sedimentation owing to 4th- and 5th-order glacio-eustatic fluctuations (Read, 1995). The widely accepted reciprocal sedimentation components of the cycles are 1) siliciclastic bases, represented by lowstand systems tract (LST) exposure, bypassed or incised siliciclastics of the

platform, and early transgressive system tract (TST) reworking; 2) shallowing upward carbonate vertical succession, indicating TST resurgence of carbonate factories at platform and highstand systems tract (HST) compensation of accommodation (Kerans and Harris, 1993; Tinker, 1998; Osleger and Tinker, 1999). Recent work by Xu (thesis in progress) also reveals regressive systems tract (RST) between the HST and LST.

A high-frequency sequence framework was proposed by Tinker (1998) for the Yates and Seven Rivers formation in McKittrick Canyon. In terms of his work, high frequency cycles which are regarded as fundamental stratigraphic building blocks are analogous to siliciclastic parasequence but contain both a deepening and shallowing component. The hierarchal framework consists of, from higher order to low, high frequency cycle, cycle set, high frequency sequence (HFS) and composite sequence (CS), which is analogous in scale to fifth-order cycles, fourth-order cycles, intermediate order cycle and third-order cycles respectively (Figure 4). The Seven Rivers, Lower Yates, and Upper Yates-Tansill Formations represent third-order CSs, respectively, and each contains four fourth-order HFSs (SR1-4 HFSs, Y1-4 HFSs, and Y5-6/T1-2 HFSs, respectively (Figure 5). According to Tinker (1996, 1998) and Kerans and Tinker (1999), the three CSs are correlated with the basin equivalents: Manzanita, Hegler and Pinery carbonate members of Cherry Canyon and Bell Canyon formations are identified within SR1, SR2 and SR4 HFSs respectively; Rader is identified within Y3-Y4 HFSs; McCombs, McKittrick and Lamar is identified within Y5, Y6 and T1 respectively.
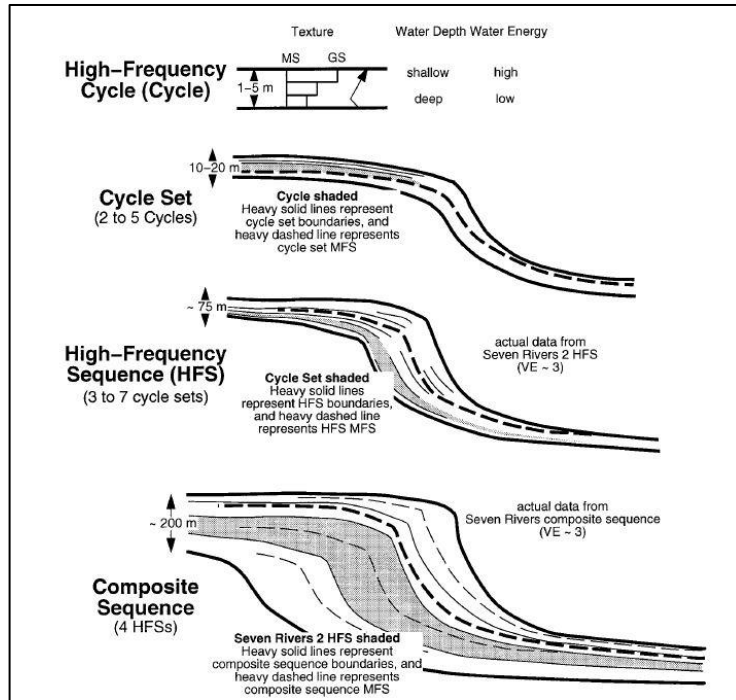
Figure 4: Illustration of hierarchy of cyclicity. Modified from Tinker (1998).
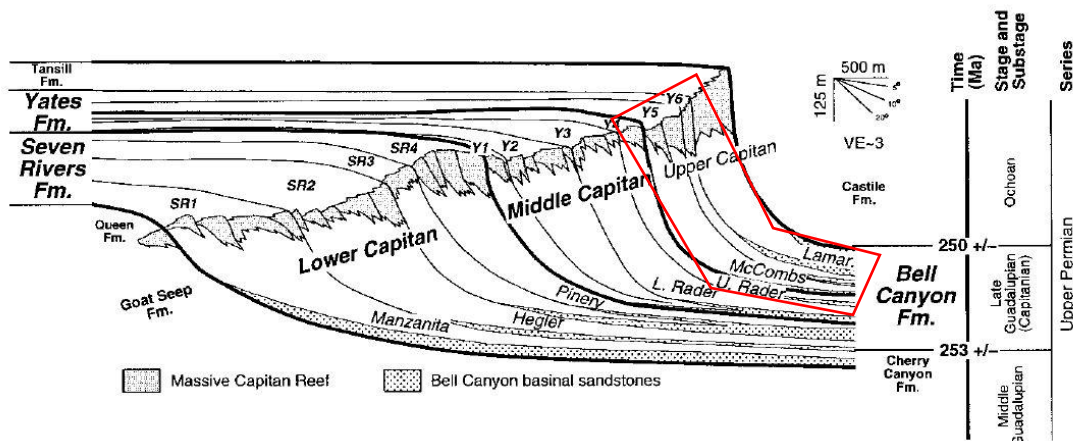
Figure 5: Simplified depositional profile of Upper Guadalupain. Three Composite Sequences (CS) are bounded by heavy line. Correlation of HFSs and Bell Canyon basinal equivalent is illustrated through the HFS boundaries. HFSs across the north wall of McKittrick Canyon are marked with a red polygon. Modified from Tinker (1998).

CHAPTER 3: METHOD

LiDAR

Introduction

Light Detection and Ranging (LiDAR), as a relatively novel technique, has been developed to be utilized in geoscience research, especially in outcrop study topics, for only decade since several revolutionary advances had been made by Bellian and Pringle (Bellian et al., 2005; Pringle et al., 2006 and in thesis by Garrett, 2015, Giddens, Hornbuckle, 2017) who applied LiDAR systematically in the studies of outcrop stratigraphy, lithofacies and mineralogic identification and reservoir characterization. In this forward seismic model investigation, LiDAR is used as a powerful tool to accurately capture the complexity of the stacking patterns of shelf-to-basin deposits, the depositional dip and strike continuity of target outcrop unit, and the 3-D geometry of the outcrop exposed in the study area, which further provide a digitalized stratigraphic model and a 3-D virtual realistic outcrop model as an aid to model construction.

The LiDAR data for this study was collected by a RIEGL VZ-400i 3D terrestrial laser scanner with a collaborative Nikon D810. This scanner can collect millions of points in one scan task with the range of up to 800 m and the resolution of up to 3 mm, forming a "cloud" of points that approximate the target space (RIEGL, 2012). A measure of single point commences with a laser pulse emitting from the scanner which travels to a remote object. The off-bounced pulse returns to the detector with the precise two-way travel time and other attributes recorded. Multiplied by the speed of light in air corrected for humidity and barometric pressure, one half of recorded travel time with angle of emission can be used to calculate the distance and coordinate of the point

where the pulse bounced, the x, y, z location relative to the referred coordinate system. Numerous points that record the coordinate and attributes will generate a point cloud of target area which covered the surrounding space. A high-resolution point cloud can characterize well the geometry of the target surface while the resolution depends on the density of the point data collected in a partigular area. The RIEGL VZ-400i terrestrial laser scanner samples a gridded point distribution, whereby a scan line is collected on one horizontal angle setting before the beam is deflected to the next line, which builds up the grid. The laser pulse emitter is set in a dedicated two-axial rotation system which can make the emitter rotate 360 degrees in horizontal plane and 30-130 degree in vertical plane (Figure 6). The RIEGL VZ-400i can also collect intensity returns, the power of the laser pulse returned divided by the emitted power, which is related to the geometry of the targeted surface and the reflective character of the object at the wavelength laser (Burton et al., 2011). The points in data volume can be painted with the true color of the object when photos are acquired by the camera that is working collaboratively at the same time with the scanner which generates a 3-D virtual realistic model of the target. The 3-D point cloud data and virtual realistic model that results helps guide the stratigraphic and depositional facies interpretations and constrain a digitalized stratigraphic frame of the outcrop for the forward seismic model.
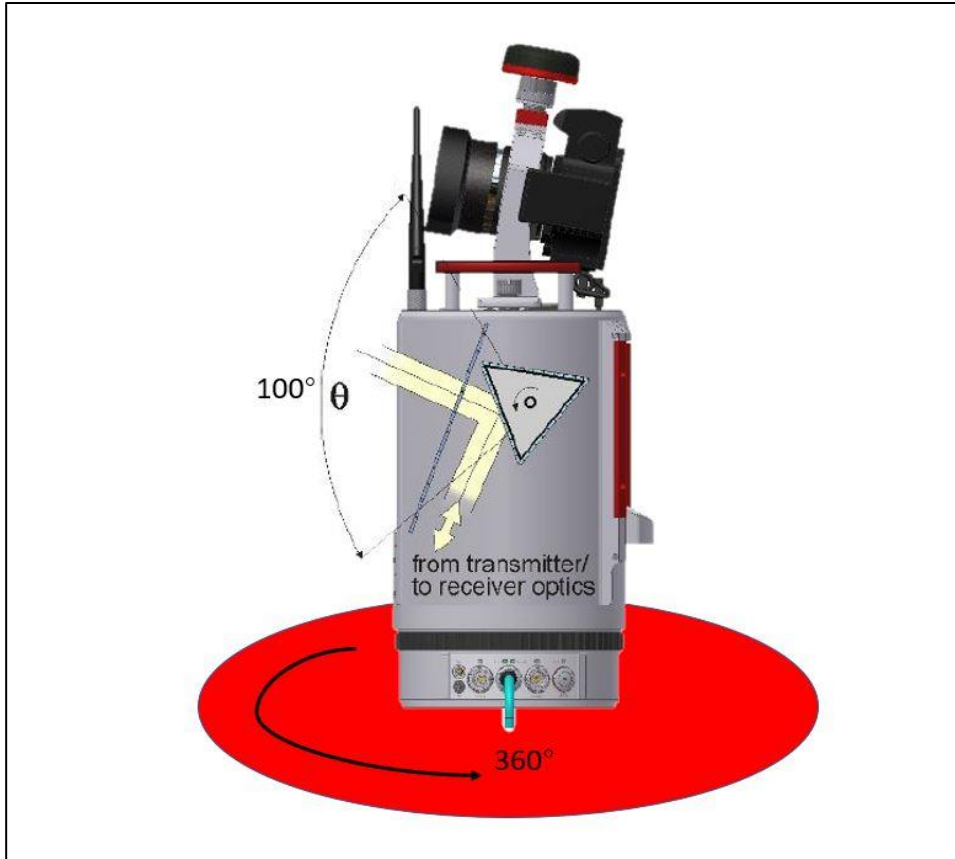
Figure 6: Scanner beam path at horizontal and vertical plane.

Acquisition in McKittrick Canyon

Since LiDAR data acquisition in the field, especially in the remote area, has a high demand on time and physical work of the operators as a result of over 80 pounds of equipment including scanner, tripod, computers, reflective targets and vehicle battery which needs to be carried into each acquisition location, the LiDAR data acquisition is especially challenging in McKittrick Canyon owing to the topography, canyon walls, and need to minimize acquisition shadow. Therefore, the planning of locations is substantial both before and during acquisition.

For example, under the consideration of efficiency, the resolution of this study is to conduct multi-station scans which can be tied with each other. In order to ensure the best quality of combined data from limited scans, one single station should be placed relatively close and maintain normal to one part of the target area to optimize the quality of certain outcrop unit. To have the different scan position effectively tie together with minimum error, at least three common tie points, represented by either reflectors or reflective cylinders, are placed in the operation area before each scan (RIEGL, 2012). More than three is ideal. Therefore, designing a survey that is fit for our purpose is a key part of the workflow. In this study, 17 scans were taken while only 12 scans are valid for further processing. Besides the 360-degree scans, fine scans with higher resolution were taken after the full-angle scans, which targeted a selected area. Acquisition parameters of each scans are listed below (Table 2). To decrease the vertical shadow of the south and north canyon walls as much as possible, scan 12 and scan 16 were taken on the slope of the south wall and north wall respectively (Figure 7).

Scan Position	Theta	Phi	Program	Resolution (Degree)
Scan position 2	30° —130°	360°	100kHz	0.025
Fine scan	75° —118°	127° —254°	100kHz	0.015
Scan position 3	30° —130°	360°	100kHz	0.015
Scan position 5	30° —130°	360°	100kHz	0.02
Fine scan	67° —95°	1° —148°	100kHz	0.01
Scan position 6	30° —130°	360°	100kHz	0.02
Fine scan	65° —96°	243° —321°	100kHz	0.01
Scan position 7	30° —130°	360°	100kHz	0.02
Fine scan	68° —91°	68° —128°	100kHz	0.005
Scan position 8	30° —130°	360°	100kHz	0.02
Fine scan	70° —90°	54° —83°	100kHz	0.003
Scan position 10	30° —130°	360°	100kHz	0.02
Fine scan	61° —94°	132° —248°	100kHz	0.005
Scan position 12	30° —130°	360°	100kHz	0.02
Fine scan	62° —104°	12° —180°	100kHz	0.005
Scan position 13	30° —130°	360°	100kHz	0.03
Fine scan	57° —94°	90° —257°	100kHz	0.01
Scan position 15	30° —130°	360°	100kHz	0.02
Fine scan	76° —96°	258° —322°	100kHz	0.004
Scan position 16	30° —130°	360°	100kHz	0.02
Fine scan	78° —102°	190° —282°	100kHz	0.004
Scan position 17	30° —130°	360°	100kHz	0.02
Fine scan	71° —89°	3° —130°	100kHz	0.004

Table 1: Acquisition parameters of 12 full-angle scans with 11 high resolution fine scans. Theta represents the vertical range of beam and Phi represents the horizontal ranges of the beam. Resolution implies a rotation interval of vertical and horizontal plane in degrees.

Figure 7: LiDAR scan position on Google Earth looking straight down into the canyon. Scans positions are marked in yellow.

Processing

The data collected in the field were registered (input into the project and tied with project coordinate system by tie point) and then exhibited in a 3-D view in Riscan Pro, the software of RIEGL where all the processing of the raw data was then conducted. Although the merged final point cloud data of 13 360-degree scans provided the high accuracy with substantial level of detail, difficulties still remained with 1) The huge amount of the data (18.8GB) included points of undesired areas and massively overlapped features of interest and 2) Point cloud data in area obscured with vegetation.

Accordingly, the processing of the data for cleaning and decimation was needed. The detail of filter application is now discussed.

1) Octree Filter

Because of the large range of the study area, the size of the combined data is larger than required. This study applied the Octree Filter which is a build-in algorithm to optimize the amount of point data by choosing the center of gravity point to represent the primary cube. After generation of the octree filtered data, the points at the center of gravity represent the other point in one primary cube which is then set manually.

2) Terrain Filter

Manual decimation of the off-terrain points from the on-terrain points can also be time consuming, especially when the target surface is covered by irregularly distributed vegetation. The terrain filter was applied in this study for decimating the widely distributed vegetation on the canyon walls. In the work flow of the filter process, an analysis of the distance of the point from an estimated ground surface is used as the criteria to classify the "terrain" point or "off-terrain" point. This filter can be applied on other plane which is specified as reference ground surface as well.

3) Reflectance Gate

The reflectance is one of the additional attributes that the RIEGL VZ-400i provide as scanning by online waveform processing which is a target property and refers to the fraction of incident optical power (RIEGL, 2012). Given in decibels, the reflectance reading is a ratio of the amplitude of the target to the amplitude of a white flat target at the same distance, orientated orthonormal to the beam axis, and with a size in excess of

the laser footprint, where negative values indicate diffusely reflecting targets and positive values are retro-reflecting targets (RIEGL, 2012). Some study about LiDAR reflectance demonstrates the relationship of reflectance and target material: Wehr and Lohr's experiment showed a larger value of the laser returned from bare rock surfaces (Wehr and Lohr, 1999); A stronger relationship between reflectance and rock texture was demonstrated by Burton (2011) and has been demonstrated to be able to specific minerology by Gidden and others (2016). In other words, the value of reflectance is qualitatively related with the target material and can be quantitatively related with the lithofacies after data processing. Given the idea stated above, a reflectance gate was applied in this study to better illustrate the exposed rock bodies. During the processing of the raw data, a narrow reflectance gate (-3 dB to 3 dB) was found for the best illustration of the outcrop in McKittrick Canyon from area of high vegetation or high weathering with a warm-cold color bar, in which the bare outcrop is best revealed in cold color and the diffusely reflected vegetation shows in warm color (Figure 8). As showed in this figure, the continuity of strata can be clearly differentiated from the vegetation.
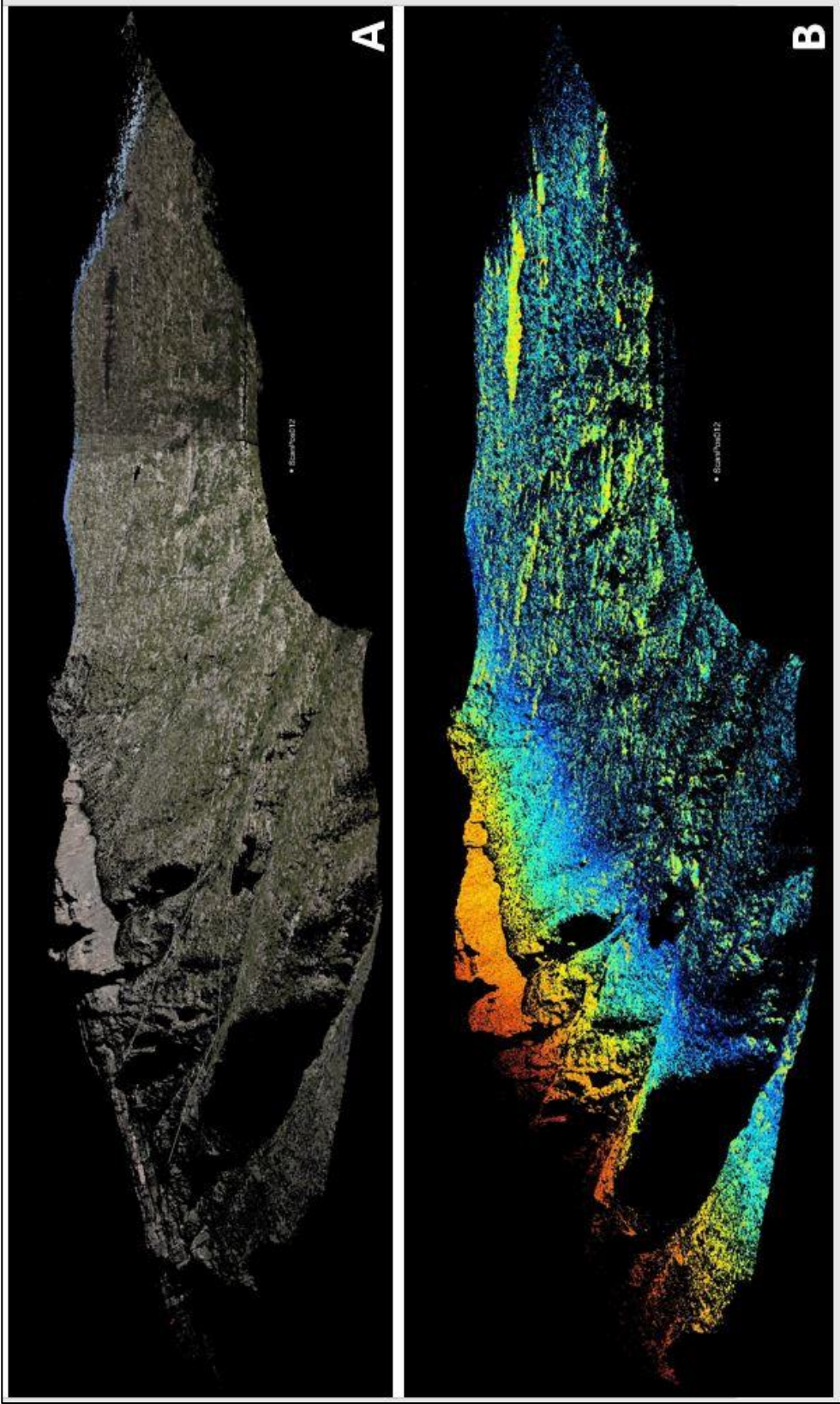
Figure 8:Comparation of point cloud data shown in true color and in reflectance with an applied filter gate. A) Point cloud data of north wall of McKittrick Canyon painted by the camera. B) Point cloud data of north wall of McKittrick Canyon displayed by reflectance with empirical set filter gate (-3.5 dB to 3.5 dB where positive values exhibited in warm colors and negative values are in cold color). Cropped out strata are easily differentiated in reflectance.

Schmidt Hammer

Introduction

Invented by Ernst Schmidt in early 1950s, the Schmidt hammer was originally developed for non-destructive testing of concrete hardness (Schmidt E, 1951). This rebound hammer has been applied in a similar manner to measure the uniaxial compressive strength of rocks from surface hardness data obtained from outcrop (Poole and Farmer, 1980). With its portability, simplification of operation and affordability, the Schmidt hammer allows the efficient estimate of the mechanical properties of rock without having to sample the rock and bring it back to lab. Despite the high accuracy of laboratory testing, the data from Schmidt hammer is acceptable in consistency and repeatability (Poole and Farmer, 1980).

The Proceq Silver Schmidt hammer is used as an indirect method to obtain P-wave velocity from the outcrop exposed in the McKittrick Canyon walls. Differing from the traditional mechanical Schmidt hammer which measured rebound number "R" and which required an impact direction correction (Impact Test Equipment, 2018), the electronic Silver Schmidt records the velocity ratio of impact to rebound number (Q) instead of the Schmidt Rebound Number (R). Winkler and Matthews (2014) explored the possibility to establishing a numerical conversion factor for Q and R by comparing the performance of Silver Schmidt and traditional mechanical Schmidt hammer and empirically derived:

where Q represents velocity ratio of Silver Schmidt and R represents the rebound number of mechanical Schmidt hammer.

$$R = 1.0182Q - 9.7625 \ (R^2 = 0.9996)_{(Winkler\ and\ Matthews,\ 2014)} \qquad (1)$$

As a result of the strong relationship between Schmidt Rebound Number (R), also called as Schmidt hardness, and mechanical properties of tested rock, many studies have been published on the quantitative definition of a series of relation which contributed to better estimation of mechanical attributes by this tool. Katz proposed correlations between rebound readings and lab-measured Young's modulus, uniaxial compressive strength and density of seven types of rock (Katz et al., 2000). A relationship between the Schmidt hardness and elastic modulus, uniaxial compressive strength and index properties of nine types of rock was introduced by Saffet Yagiz (Yagiz, 2009). Comparison between different types of Schmidt hammers and the quantitative classification of weathering grades by rebound number was made by Aydin and Basu (Aydin and Basu, 2005). The empirical equations for predicting P-wave velocity by Schmidt hammer rebound number was developed by Sharma and Singh (2011) who analyzed the rebound number of Schmidt hammer on different type of rocks. A high reliable correlation of the predicted P-wave velocity and the lab-measured velocity was found when applying this empirical equation.

$$V_{p-wave}(m/s) = 966.22e^{0.0262R} \ (R^2 = 0.9584)_{(Sharma\ and\ Singh,\ 2011)} \qquad (2)$$

where R represents the Schmidt rebound number while V_{p-wave} represents P-wave velocity. Combining the Sharma and Singh relationship of equation (1) and Winkler and Matthews's equation (2), a relation between V_{p-wave} and Q is:

$$V_{p-wave} = 966.22e^{0.02667684Q-0.2557775} \qquad (3)$$

This equation is applied in this study for estimate the P-wave velocity of outcrop. A work flow for indirectly predicting P-wave velocity by Silver Schmidt reading Q is showed below (Figure 9).
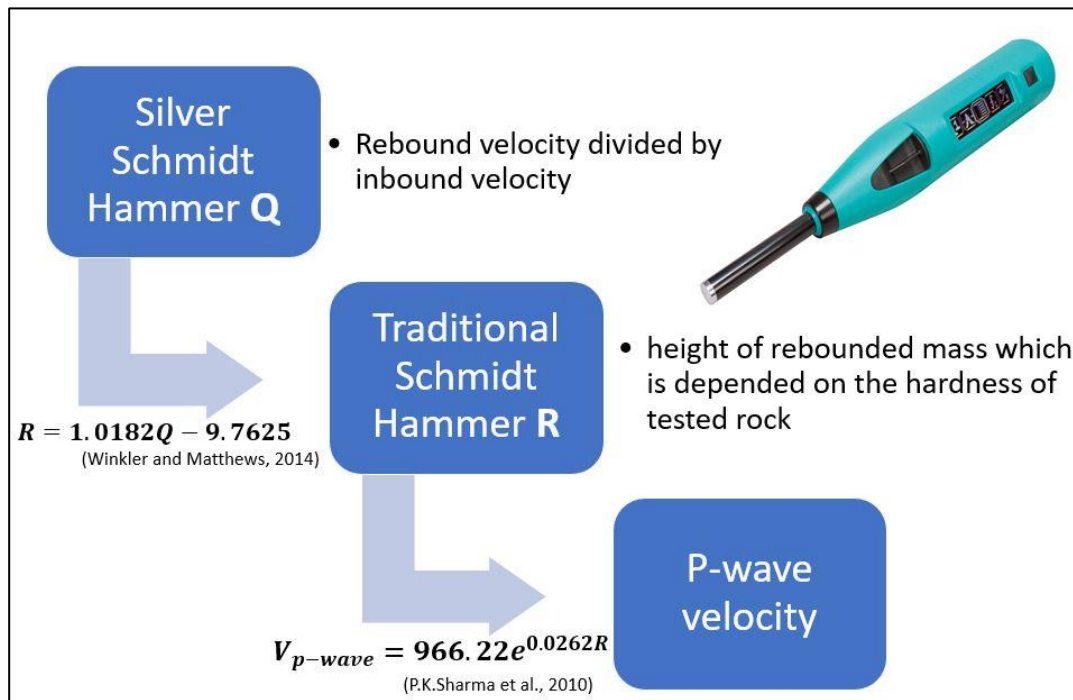
Figure 9: Work flow of estimating P-wave velocity by velocity ration Q obtained by Silver Schmidt hammer. By two steps, P-wave velocity can be estimated from velocity ratio Q.

Acquisition in McKittrick Canyon

To make the estimated velocity data set full and adequate for velocity analysis across the whole section of the study area from shelf to the most distal slope deposit, the

acquisition survey of Schmidt hammer with sample collection was designed to obtain

the data from all accessible area for investigator of both side of the canyon. A total of

125 data sets, including Schmidt hammer readings and rock samples collected for

subsequent density analysis, were obtained with 37 samples from the south wall and 88

samples from the north wall (Figure 10). For the south wall, 17 readings were taken at

strata that can be distinguished by lithofacies and 20 were taken along the ridge from

creek to south wall top with a 10-meter interval. The data took from north wall includes

33 data sets from the ramp close to the mouth of canyon and 55 data sets from Permian

Reef Geology Trail (Figure 10).
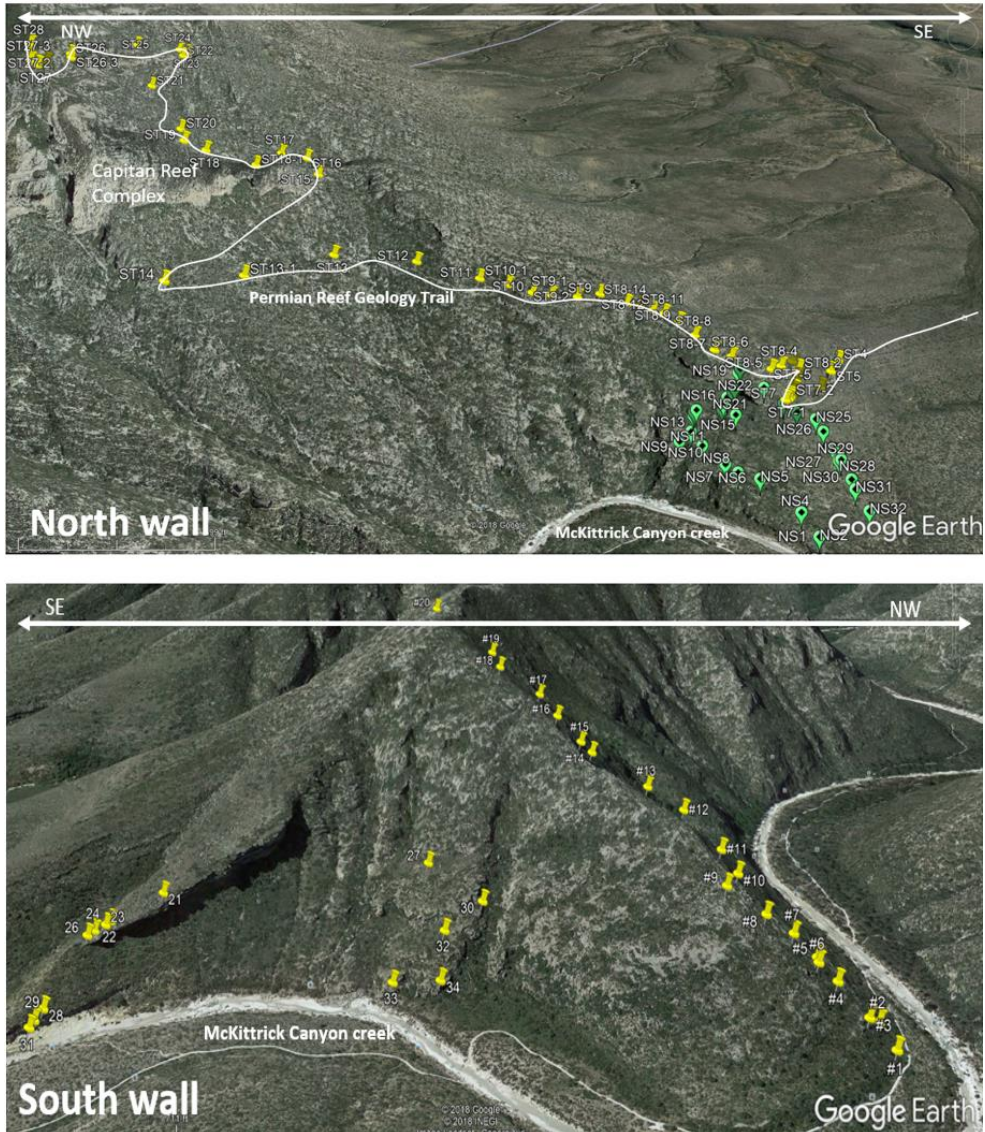
Figure 10: Schmidt hammer and rock specimens sampling position at north wall of south wall of McKittrick Canyon.

The Proceq Silver electronic Schmidt hammer records the data in its built-in memory unit. Five optional settings are provided by Proceq Silver Schmidt hammer which are listed below:

1) Units:

   Q, kg/cm^2, N/mm^2, psi and MPa is available while Q is selected for all acquisition

2) Statistics

Regional, Median, Mean and User preset is available while Mean was selected

for all acquisitions which required 10 impacts from which a mean is calculated.

The series is invalid if more than 20% of the values differ from the mean by

more than 6.5 Q.

3) Conversion curve

10th percentile, Reference, Custom curve is available while 10th percentile was

set for all acquisition in this workaaaa

4) Form factor

Cylinder, Standard cube, User defined is available while Standard cube was

selected for all acquisition.

5) Carbonation correction factor can vary from 0 to 1.00

0.5 was set for all acquisition in this work

In order to avoid effects of weathering, all readings were taken on either a fresh surface
or on an unweathered zone of the outcrop.

Data Set

12 full-angle LiDAR scans with 11 high resolution fine scans were taken at
McKittrick Canyon, which characterizing the whole canyon with photograph painted
point cloud (Figure 12).

125 sets of Q values were taken by Silver Schmidt hammer, which are represented by
the mean value of readings from 10 impacts. Standard deviation of each data sets ranges

from 0.5 to 5, implying the validity of all data. Most value range from 50 to 70 which is taken from carbonate or unweathered siliciclastic units while readings below 50 were usually taken from weathered zone and shale, whose readings are even lower down to 20. More details of data analysis are discussed at Result chapter.

120 rock samples were collected at the same locations where the corresponding Schmidt hammer readings were obtained. The Ohaus Adventure Balance with density measurement kit is utilized in this study for efficient measuring of rock sample densities (Figure 11). The density determination is performed by the Archimedes' Principle that every solid body immersed in a fluid apparently loses weight by an amount equal to that of the fluid it displaces. By measuring the weight of each sample in air and in water, bulk density of samples is calculated through built-in density measuring program of Ohaus Adventure Balance and displayed directly on the screen.

Figure 11: Ohaus Adventure Balance with density measurement kit.

Figure 12: McKittrick Canyon photograph painted point cloud which ties 12 full-angle

CHAPTER 4: RESULT

LiDAR assisted stratigraphy model

Stratigraphy frame of the shelf-to-basin deposit at the north wall of McKittrick Canyon is interpreted on Riscan Pro based on the processed LiDAR point cloud. Based on the stratigraphic background which is discussed in the introduction chapter and the understanding from field reconnaissance, the Late Guadalupian shelf to toe of slope at north wall of McKittrick Canyon represents a mixing carbonate-siliciclastic depositional system where four HST carbonate members interfinger with three bypassed LST siltstone and sandstone wedge. More detail of stacking pattern of these units can be viewed from post processing results of point cloud data.

As the youngest unit which is visible at McKittrick Canyon, the mostly eroded Reef Trail Limestone members only displays 4m thickness above the Lamar Limestone, overlying the youngest Lamar member concordantly. The Lamar Limestone member is visible from both wall of the canyon, cropping out as enormous bare cliff at the south and wedge-shaped exposures at the north, which provides a reference unit for interpretation. Lamar limestone is slope equivalent member of T1 HFS which is divided into six higher order cycles by surfaces which show a systematic pattern of bed termination (Figure 13 A). From bottom to top, the six units are name with Lamar unit 1 to Lamar unit 6 respectively. Lamar unit 1 appear only at distal part of slope, pinching out towards up-dip, which terminates as onlap against underlying LST Sand C. Downlapping occurs in Lamar unit 2 against underlying Lamar unit 1. Lamar unit 3 represents conformity with overlying and underlying strata and slightly thickening

31

towards basin. Similar to unit 1, Lamar unit 4 is absent at upper and lower slope,

representing on-lap against underlying Lamar unit 3 at toe-of-slope. Downlap occurs in

Lamar unit 5 against Lamar unit 4, pinching out basinward. Lamar unit 6, as the

youngest unit in Lamar member, represents conformity with underlying units. Higher

frequency cycles cannot be identified from LiDAR for the rest of HFSs, the McKittrick

Canyon, McComb and Rader member, all of which shows the tendency of basinward

thinning. Onlapping occurs at all three siltstone wedges against underlying unit, which

is interpreted as bypassed siliciclastic from the shelf of LST (Figure 13 B). The

stratigraphic frame of McKittrick Canyon north wall is displayed in Figure 14, where

eroded reef and HFS boundaries traced to shelf is reconstructed.
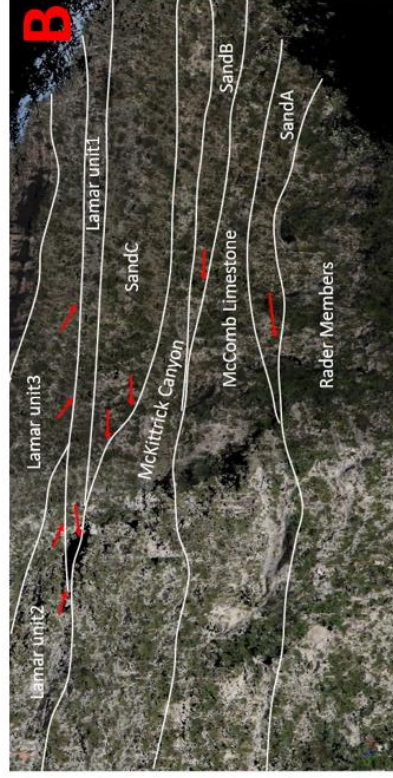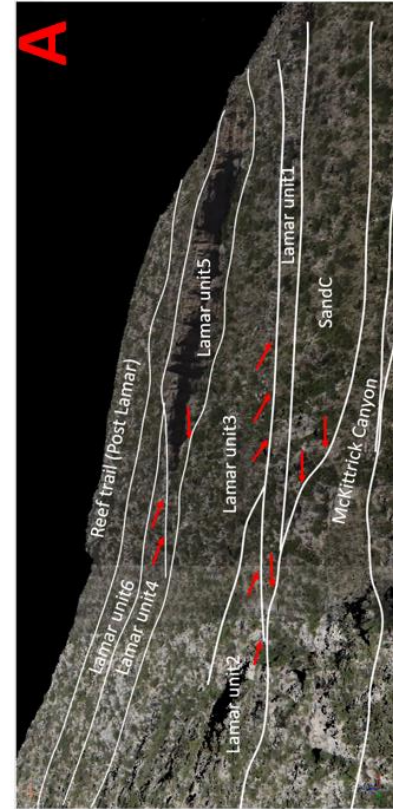
Figure 13: True color painted point cloud of McKittrick Canyon north wall. Detail of unit stacking can be viewed in enlarging box A) high frequency cycles in Lamar Member B) interbedding of siliciclastic onlapping wedge and HST carbonate members.
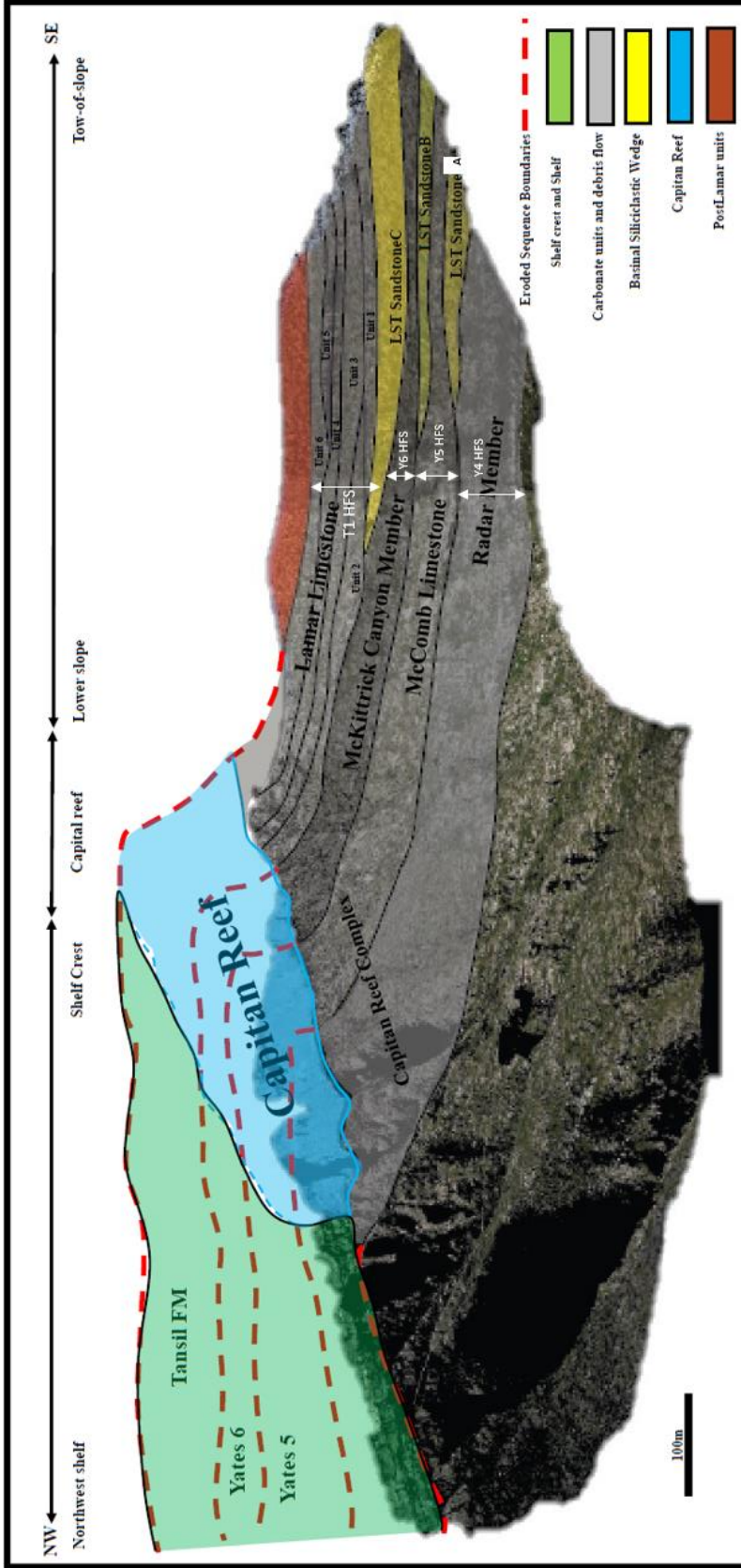
Figure 14: Stratigraphic frame of north wall of McKittrick Canyon on LiDAR data. Eroded surfaces and units of Capitan reef and shelfal deposit are reconstructed, presenting a mixing carbonate-siliciclastic depositional system where four HST carbonate members interfinger with three bypassed LST siltstone and sandstone wedge.

Impedance model

Data set analysis

The acoustic impedance applied in this work is from the product of P-wave velocity and dry bulk density. 125 groups of data, including Schmidt hammer reading Q and corresponding bulk density measured by rock sample, were collected at the both wall of McKittrick Canyon. The Gardner Equation, proposed by Gardner and others at 1974, built a relationship of rock's bulk density and P-wave velocity with data from a wide range of basins, geological ages and depth, providing a general link for estimating one value from another. Compared to the Gardner relations (Figure 15), these data clearly demonstrate the variability of carbonate from a simple density-velocity empirical relationship owing most likely to change in the elastic model caused by change in the limestone carbonate/clastic fraction. Xu (unpublished thesis) shows from XRF elemental analysis the heterogeneity in carbonate composition.
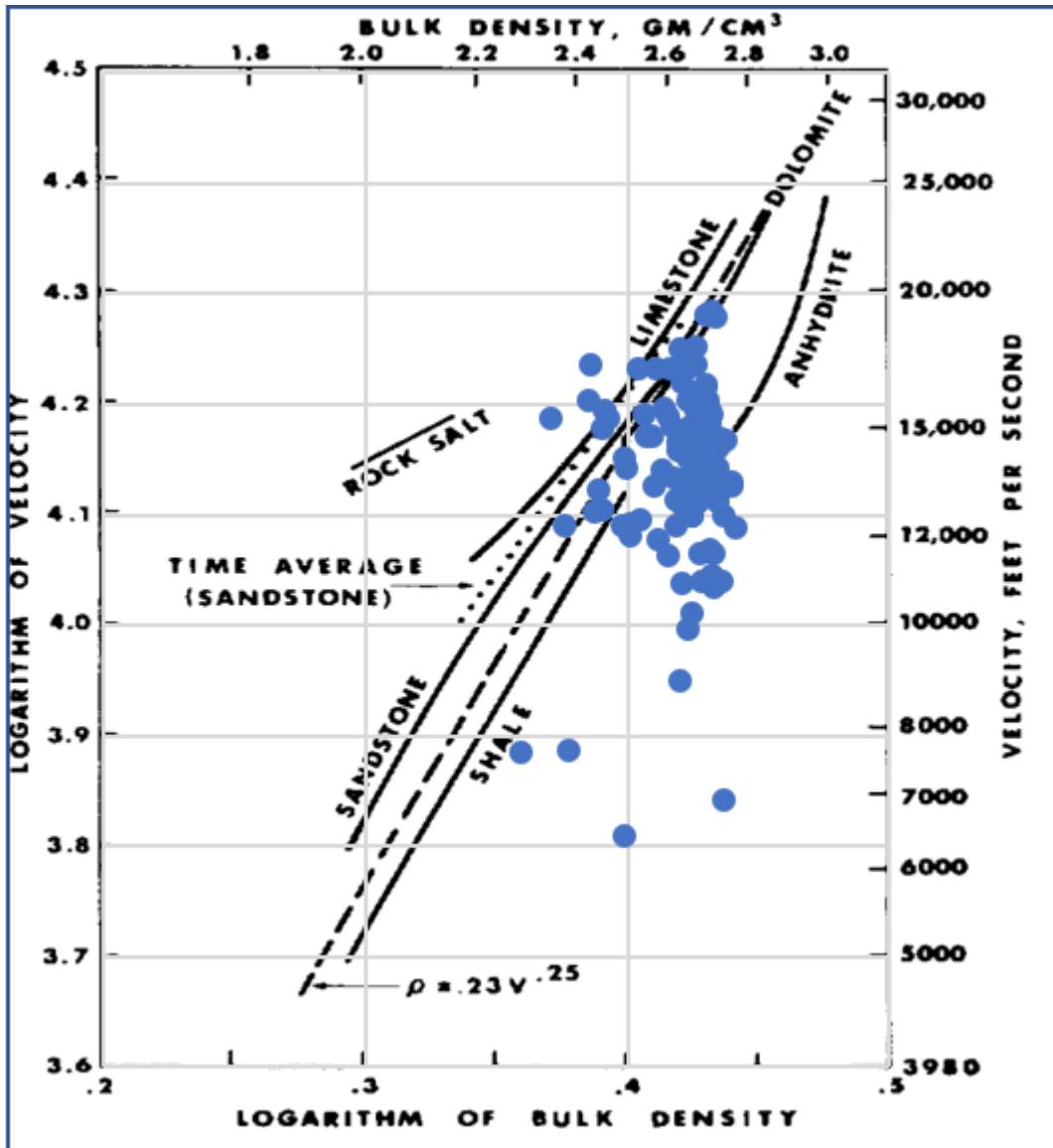
Figure 15: Data set collected at McKittrick Canyon compared to Gardner's relationship with data plotted in logarithm. Unit of P-wave velocity is in ft/s while unit of density is in g/cm^3. Graph is after Gardner (1974).

For each group of data, the GPS location is used for matching of the sample

location with its corresponding position on LiDAR point cloud. Based on the

stratigraphic model of the slope profile, each group of data is interpreted by the stratal

unit where the data is positioned. The strata units with multiple sampling at different

positions indicate the heterogeneity of the velocity and impedance distributions along

the profile. The projected distance from the most distal point of shelf, can be used as an index to characterize the relative position of sediment. The along-slope distance of every sample calculated by corresponding GPS location is rescaled into 0 to 100, when the zero represents the most proximal location and the larger number indicates the more distal location along the slope.

P-wave velocity and acoustic impedance of units with wide lateral extension are analyzed by cross plotting impedance versus the rescaled along-slope distance. Note that the trend of velocity changing along the slope is high correlated with the impedance variation trend in every unit, which indicates that velocity has a dominant impact on the calculation of acoustic impedance when multiplied by corresponding density. Both velocity and acoustic impedance shows a weak increase towards the basin at Rader Limestone, McComb Limestone and Lamar unit 3 (Figure 17, 20, 23) while impedance and velocity of McKittrick Canyon member, Lamar unit 2, Lamar unit 4, Lamar unit 6 and Post Lamar member tend to decrease from proximal distal slope. (Figure 16, 18, 19, 21, 22).
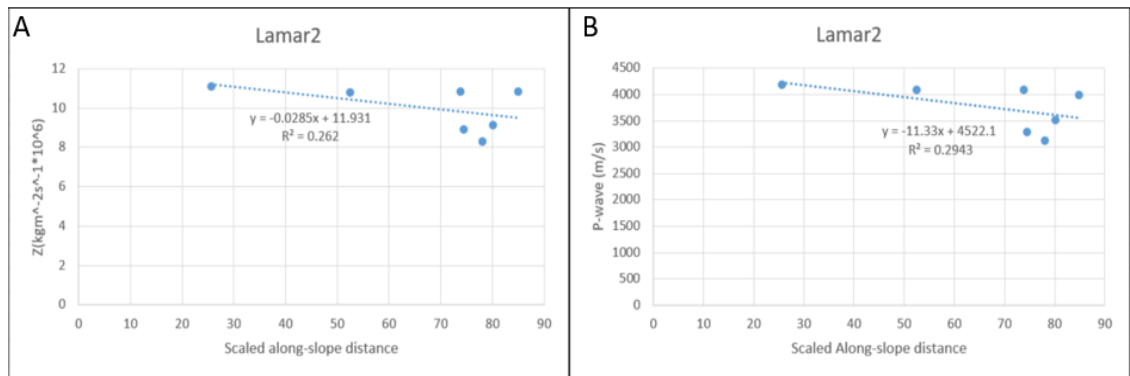
Figure 16: Cross plotting of scaled along-slope distance with acoustic impedance(A) and velocity(B) of Lamar unit 2.
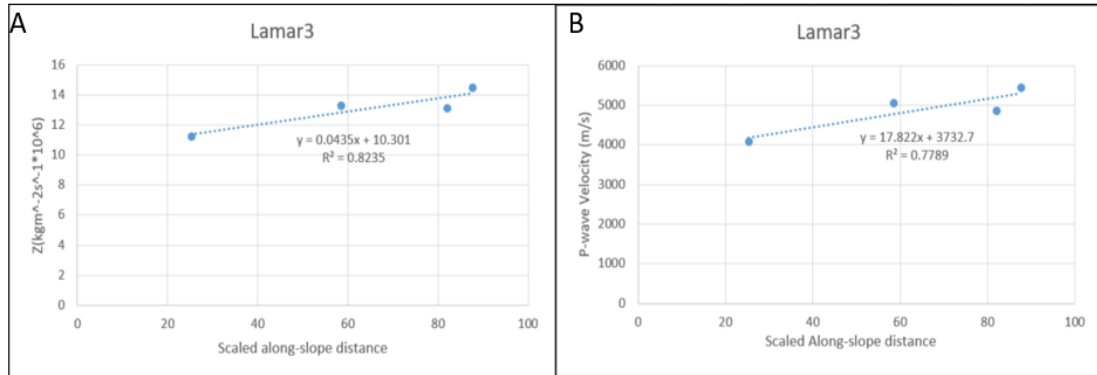
Figure 17: Cross plotting of acoustic impedance(A) and velocity(B) with scaled along-slope distance of Lamar unit 3.
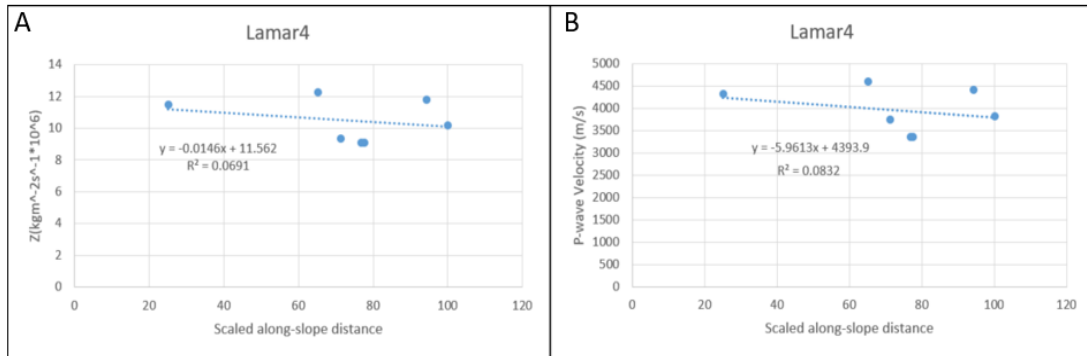
Figure 18: Cross plotting of acoustic impedance(A) and velocity(B) with scaled along-slope distance of Lamar unit 4.
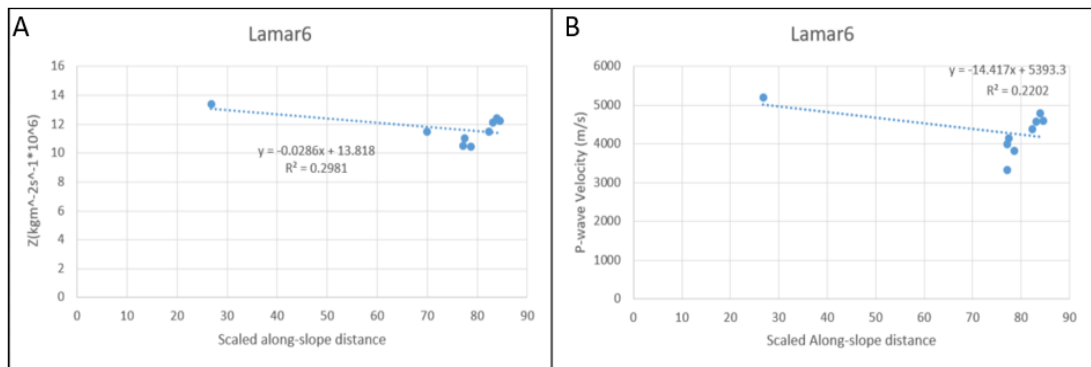
Figure 19: Cross plotting of acoustic impedance(A) and velocity(B) with scaled along-slope distance of Lamar unit 6.
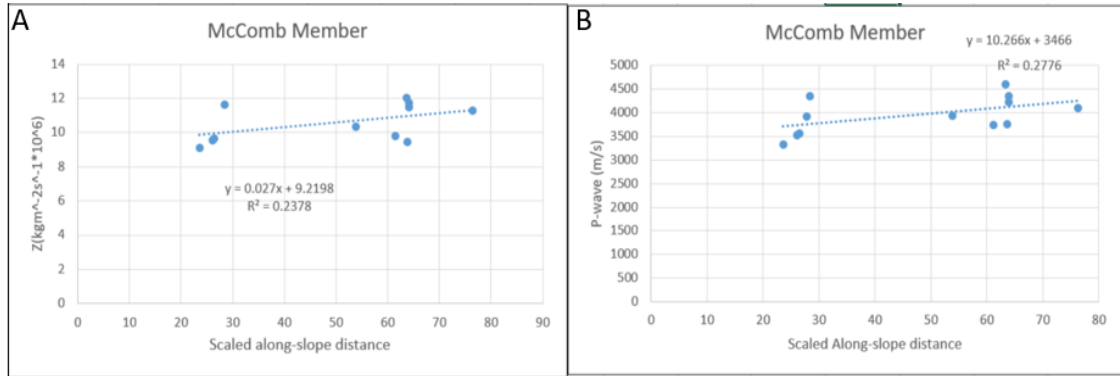
Figure 20: Cross plotting of acoustic impedance(A) and velocity(B) with scaled along-slope distance of McComb Member.
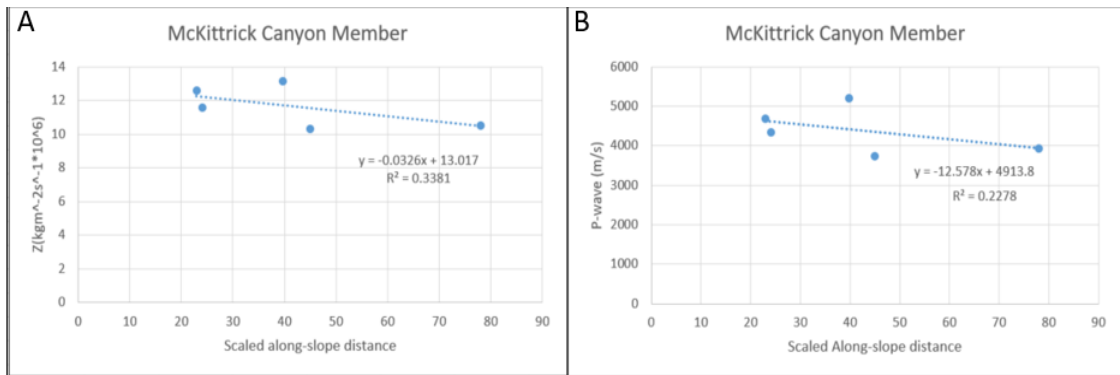
Figure 21: Cross plotting of acoustic impedance(A) and velocity(B) with scaled along-slope distance of McKittrick Canyon Member.
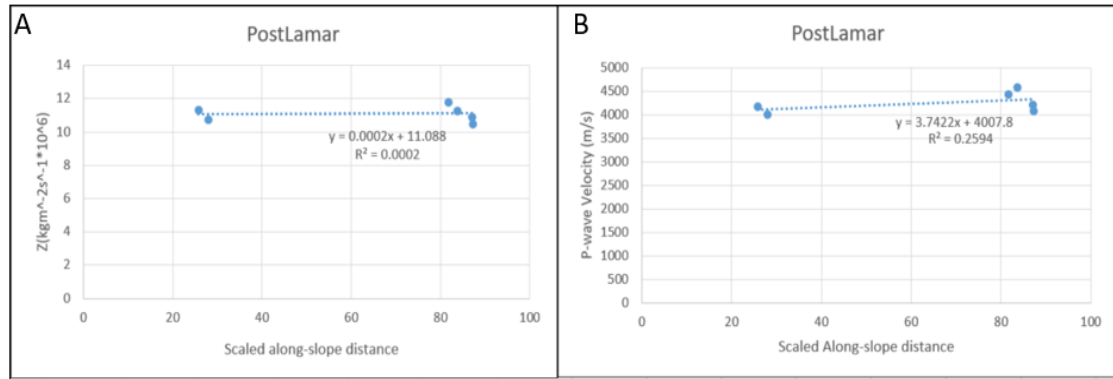
Figure 22: Cross plotting of acoustic impedance(A) and velocity(B) with scaled along-slope distance of PostLamar (Reef Trail Member).
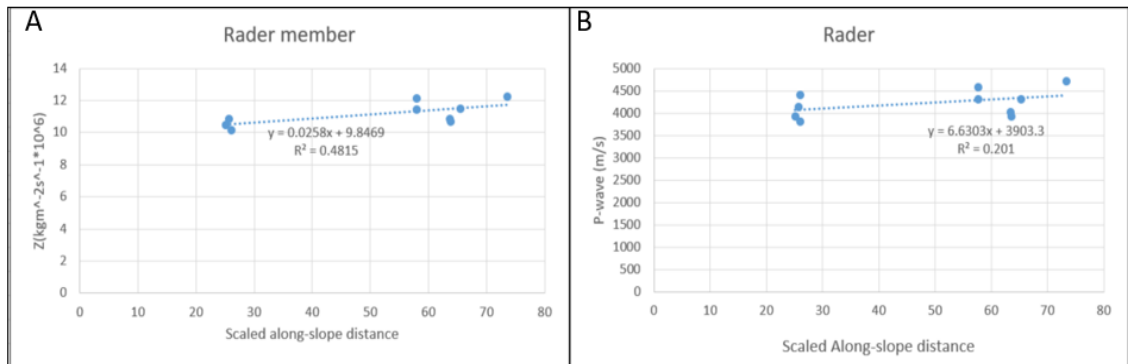
Figure 23: Cross plotting of acoustic impedance (A) and velocity (B) with scaled along-slope distance of Rader Limestone.

Depth and velocity model

To conduct the forward model, first a depth model is constructed and then an impedance model is built from the stratigraphic model which was interpreted in Riscan Pro and exported as a dxf file with recording of the location coordinate of every node on the stratigraphic polyline. The projected positions of all sampling point on 2D stratigraphy frame are showed in Figure 24 where red stars represent data position sampled along Permain Reef Geology Trail and green triangles represent data collected at south wall which are projected on north based on along-slope distance interpretation

40

(Figure 23). According to the stratigraphy frame, velocity is assigned to each stratum based on analysis of velocity distribution (Figure 25).

Impedance Model

Based on the stratigraphy interpretation, the acoustic impedance is assigned to each stratum in accordance with trend line equations while Sand A, Sand B, Sand C, Capitan reef, and shelfal strata are filled with constant impedance. The resulting impedance model is subsequently configured, resulting in a mesh of rectangular constant impedance cells. (Figure 26).
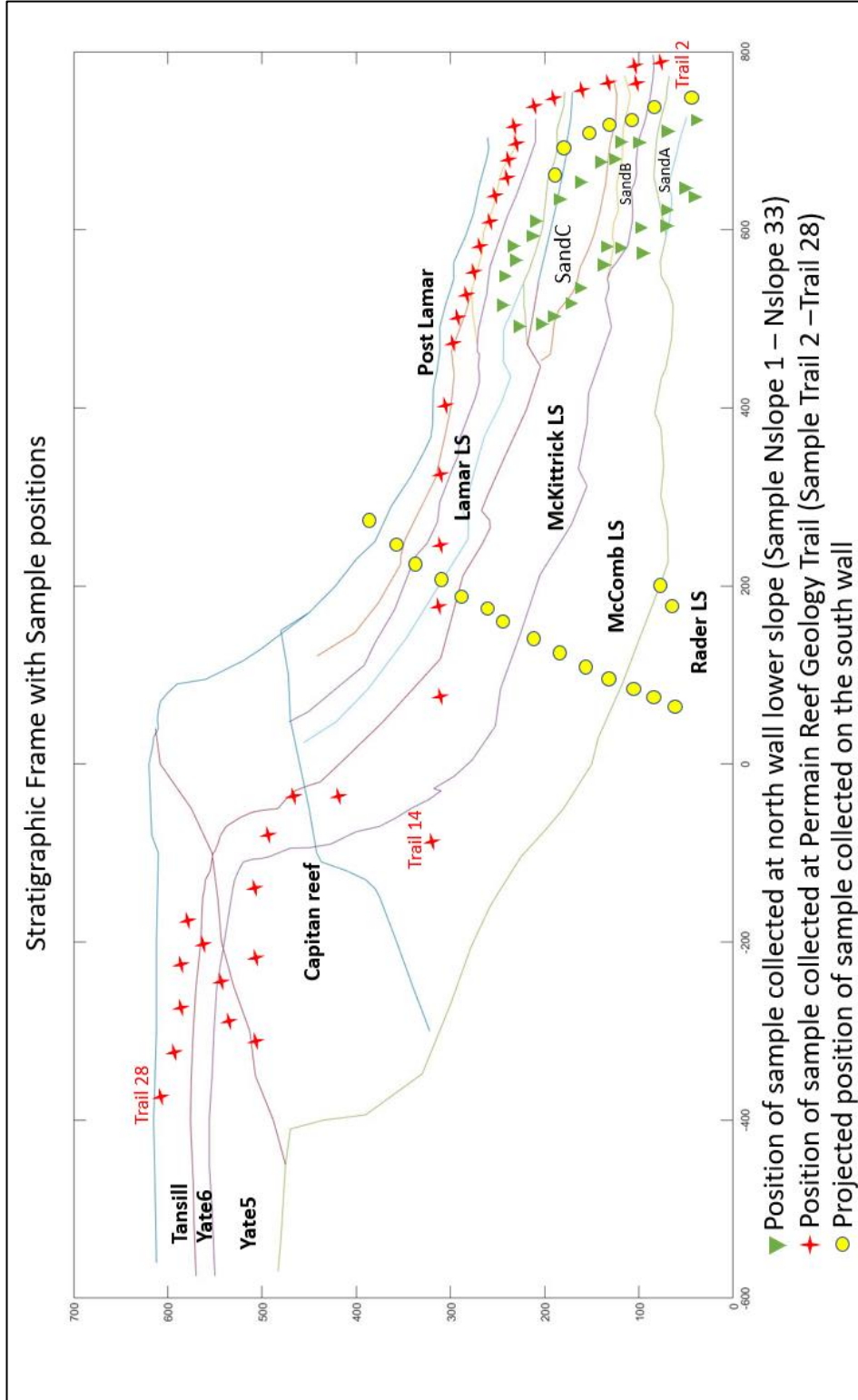
Figure 24: 2D stratigraphy frame with projected sample positions. Note that the sampling positions cover the study area
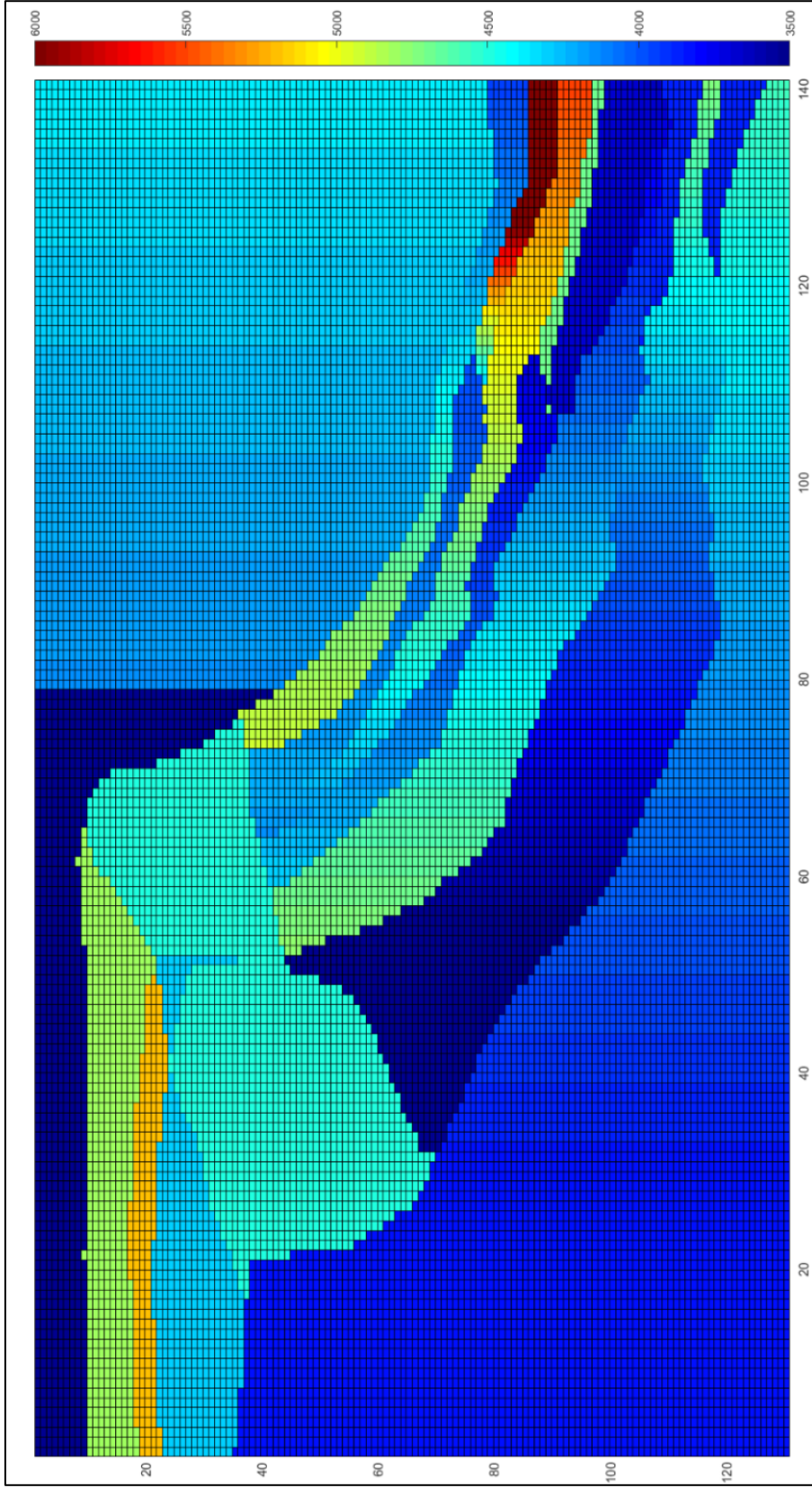
Figure 25: Velocity model of study area. Note that the average velocity of Lamar HFCs is higher than overlying and underlying strata and velocity of carbonate unit is inconsistent along the slope.
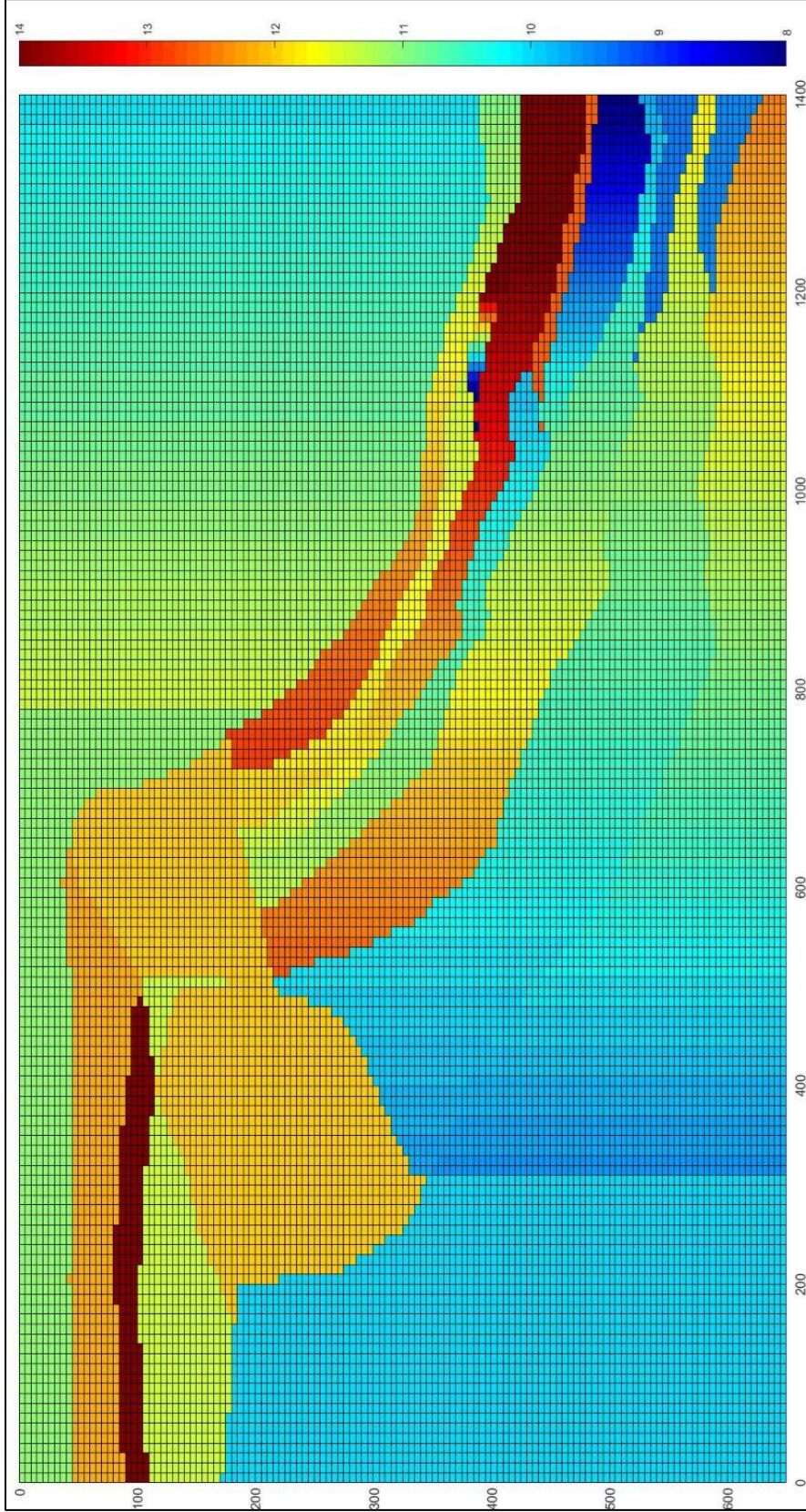
Figure 26: Calculated acoustic impedance model built upon the stratigraphic depth model of Figure 23. Note that those carbonate units documented in this clinoform perform higher impedance than siliciclastic units do. The gradual changing of impedance of one single unit is implied by lateral color shifting.

44

Seismic Model

The vertical-incidence method that uses a Matlab written program (see Appendix II) is utilized to convolve the reflection coefficients with a band limited Ormsby wavelet (Equation 4).

$$RC * W_{input} + N_{gaus} = S + N_{gaus} \qquad (4)$$

where RC represents the normal incidence reflection coefficient, W is the Ormsby filtered zero-phase input wavelet, N the Gaussian noise and S the forward modeled seismic line. The reflection coefficient is calculated by the ratio of the difference to the sum of acoustic impedances between the units on either side of a boundary (Equation 5).

$$RC_i = \frac{\rho_{i+1} \cdot V_{i+1} - \rho_i \cdot V_i}{\rho_{i+1} \cdot V_{i+1} + \rho_i \cdot V_i} \qquad (5)$$

where ρ_i and ρ_{i+1} are densities of the layers above and below the ith interface, respectively, and V_i and V_{i+1} are the calculated velocities from Q (Equation 3) of the layers above and below the ith interface, respectively. RC is the reflection coefficient at the ith interface.

This method generates a seismogram at each trace, in which the reflectors are in the true vertical two-way time and horizontal position with respect to the interpreted bedding plane reflectors. Traces with a 10-meter interval were placed along the 1400m-length 2D synthetic seismic line. This means every trace in the seismic model works as one-dimensional seismogram of an imaginary borehole at the location of each traces. Thus, this vertical-incidence profile in this work reveals the stratigraphic relationships and

45

amplitude features that would be resolved under ideal, migrated, relative amplitude balanced and gather trace balanced conditions. Although this method neglects problems and impact of propagation of seismic waves, it can also work well with insignificant difference in terms of simple defined model. In this study, a Ormsby trapezoid filter with three different frequency band widths and tapers are used to investigate the seismic response of stratigraphic architecture occurring in the study area under different acquisition conditions.

Forward 2D model generation, 250 Hz Nyquist

The first models using a zero-phase wavelet with the 2 8 120 250 Hz Ormsby frequencies (lowcut, lowpass, high pass, high cut respectively) are to simulate the seismic profiles whose resolution is comparable to a 2ms sample rate and 250 Hz Nyquist acquired and processed seismic under idea noise-free conditions. Contemporary seismic in the Delaware Basin commonly has a 4ms sample rate Therefore, this model well preserved the high frequency information where reflections have good correlation with stratigraphic surface and boundaries of litho-unit. By plotting in wiggle regime, this model clearly displays the waveform of every traces (Figure 27). Note that the variation of reflector strength and polarity occurs in the base of T1 HFS, Y6 HFS and Y5 HFS, implying the AI heterogeneity in each HFS and litho-unit which is the result of AI changing along the slope.

By writing the data into SEGY format with headers (Appendix II), the synthetic data was input into Petrel as a 2D seismic line and displayed where red represents positive amplitudes and blue shows negative amplitude (Figure 27, Figure 28). Figure 29 shows the interpreted profile where modeled stratigraphy frame is marked by solid

black lines ——thick and thin solid line represent HFS boundaries and HFCs in Lamar

Limestone respectively. Pseudo Capitan reef boundaries are marked by a dash line.

Under this band, the high frequency cycles of Lamar Limestone can be resolved as well

(Figure 29 A). Eustacy-caused cyclic stacking allowed unit 1 and unit 5 to terminate

with onlapping on the proximal side and unit 2 and unit 6 terminating with downlapping

on the downdip distal side. The variation of impedance between six Lamar high

frequency cycles units contribute to the differentiation.

Note that the base of T1, Y6 and Y5 HFSs, marked by thick black lines,

correspond to those reflectors whose amplitude and polarity is directly controlled by the

impedance contrast between the upper and lower units (Figure 29 B and C). The base of

the T1 HFS performs positive reflectivity with medium amplitude. The base of the Y6

HFS performs negative reflectivity with strong amplitude which attenuate basinward,

presenting a polarity shift from negative to positive at toe of slope. The base of Y5 HFS

exibites stronger amplitude with positive reflectivity at lower slope and toe of slope

than it does at upper slope. Note that the variation of polarity and strength of reflectivity

is mostly controlled by lithofacies changes on the both sides of the boundaries: stronger

positive reflectivity takes over when base of Y5 is overlying by Sand A while the

amplitude of base of T1 is slightly diminishing where Sand C onlaps against it.

However, similar changes also occur at boundaries between the Capitan Reef and

adjacent units resulting in variations of impedance contrasts.
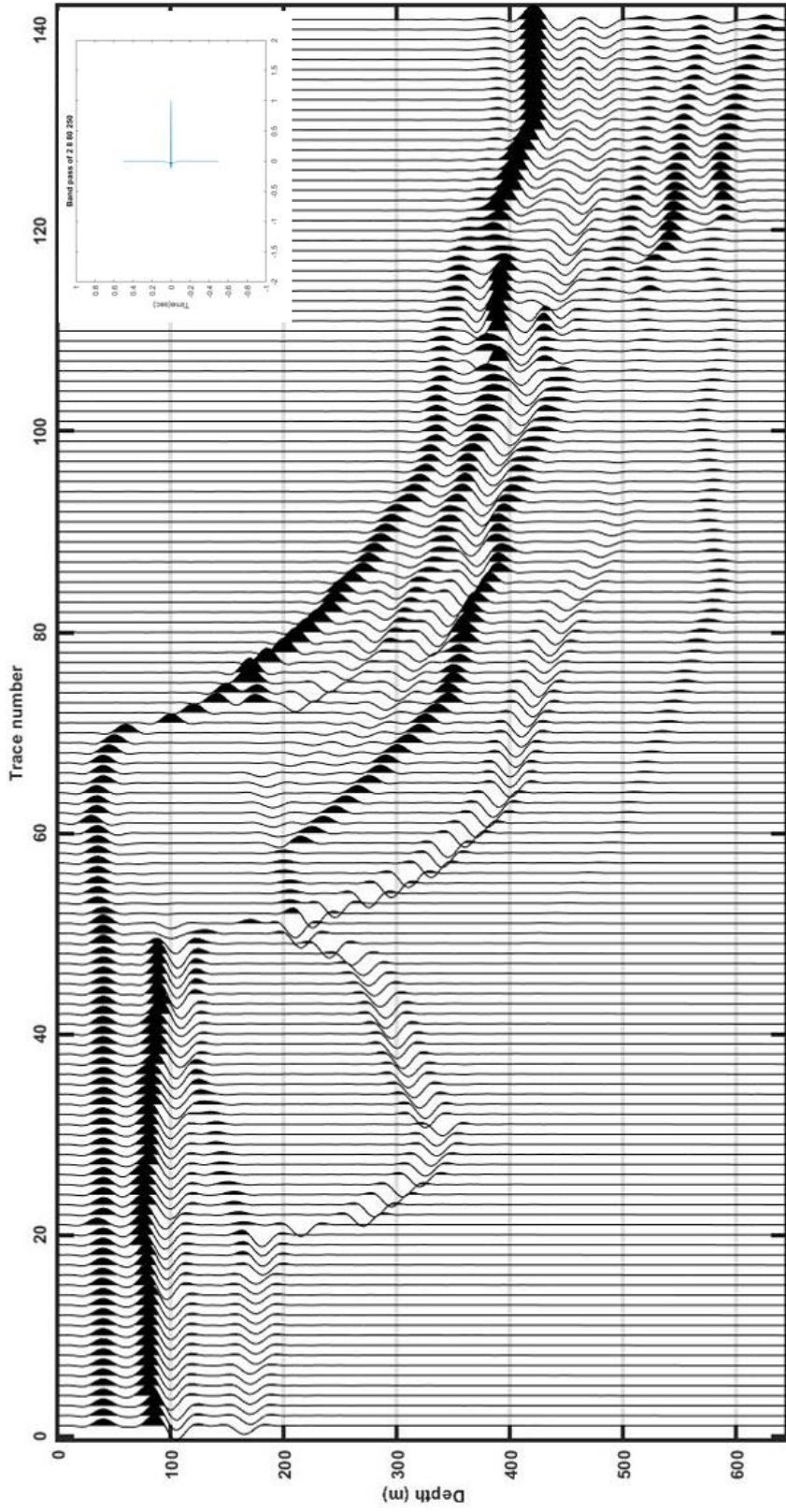
Figure 27: Wiggle plot of model with an Ormsby band pass of 2, 8, 80, 250 Hz. Peaks that represents positive amplitude are filled while unfilled troughs represent negative amplitude.
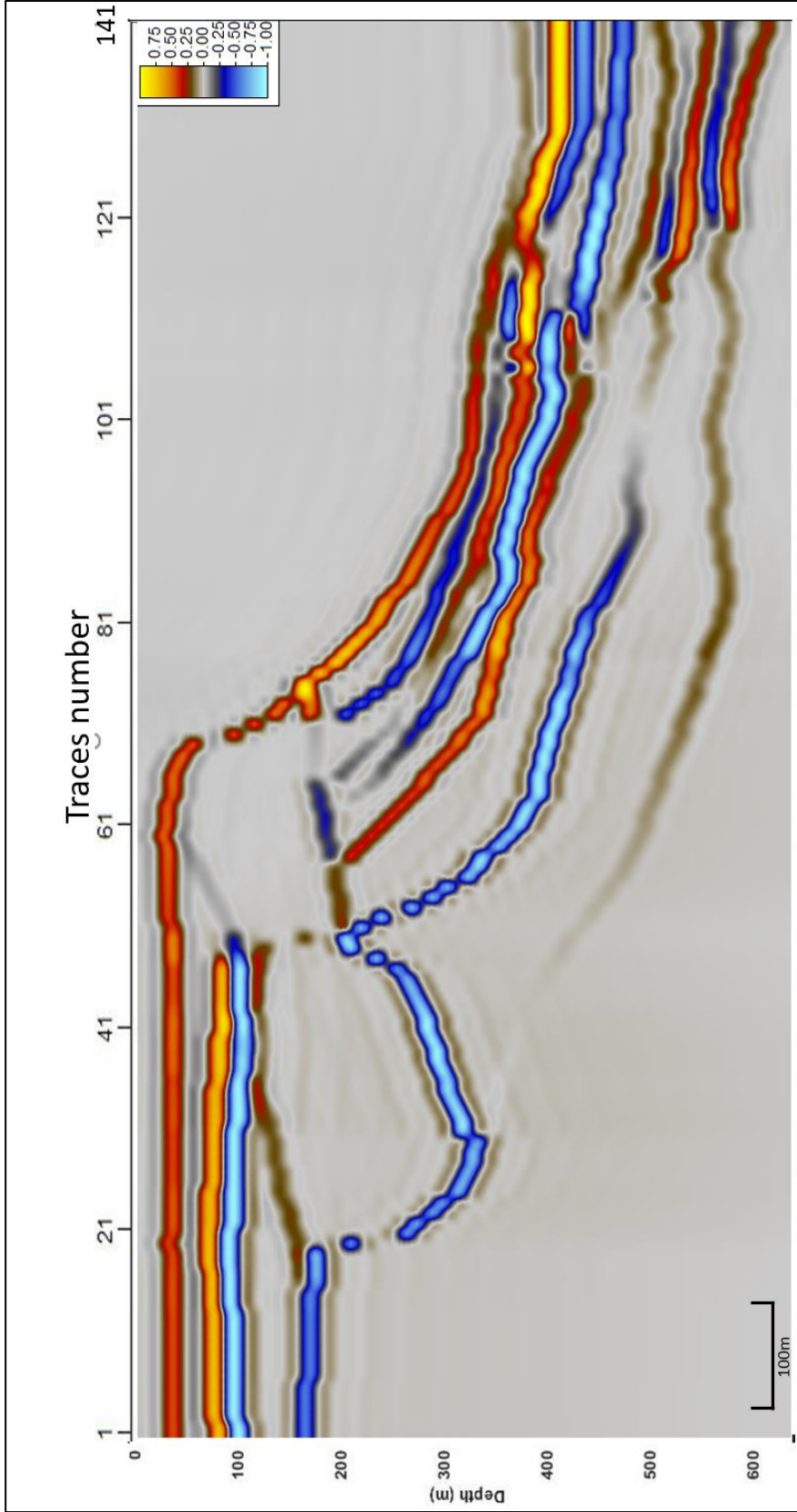
Figure 28: Synthetic seismic profile of the north wall with Ormsby band pass of 2, 8, 80, 250 Hz displayed in Petrel.

49
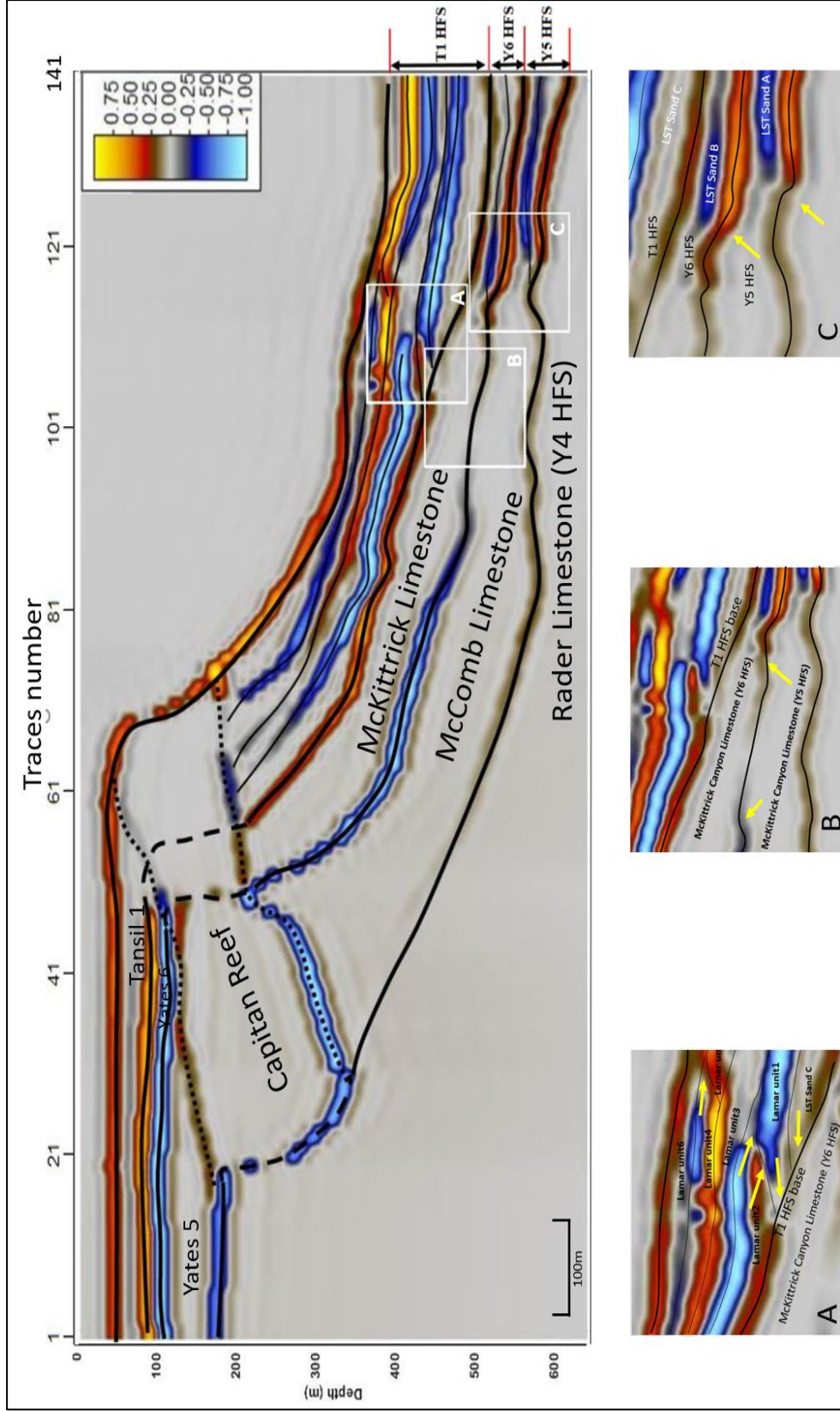
Figure 29: Synthetic seismic profile of the north wall with Ormsby band pass of 2, 8, 80, 250 Hz with stratigraphy frame and insets are marked by the white rectangles. Detailed stratigraphy architectures are displayed by A) High frequency cycles of Lamar Limestone. Featured termination is marked by yellow arrows; B) Polarity switching of base of Y6 HFS. C) Amplitude strength changing of base of Y6 and Y5 HFS at toe of slope.

Forward 2D model generation, 125 Hz Nyquist

Two more synthesizing practices are modeling by narrow Ormsby band width wavelet, one at 2, 8, 80, 125 while the other at 2 8 62.5 80. The model using wavelet at Ormsby band pass of 2, 8, 80, 125 is to investigate the ideal seismic response of this profile recorded with a 4ms sample interval (Figure 30 and Figure 31). The model that uses wavelet at 2 8 62.5 80Hz Ormsby band pass with added 5% random noise is to simulate more natural conditions (Figure 32 and Figure 33).

As to the models under the lower band width, difficulties exist for interpretation of exact position of sequence boundaries although HFS can be interpreted by distinctive reflectors. In this model, simulated thin beds are unrecognizable owing to aliasing and HFS boundaries are not well correlated with reflections. Note that the reflectors in the model synthesized by 2 8 62.5 80 Ormsby wavelet express the litho-units instead of surfaces while HFSs, therefore, are identified by litho-units instead of sequence boundaries. Reflectors of basinward thinning carbonate members such as McKittrick Canyon limestone and McComb limestone pinch out at toe of slope where their thickness dropped dramatically and the basinward thickening siliciclastic turbidites occur.
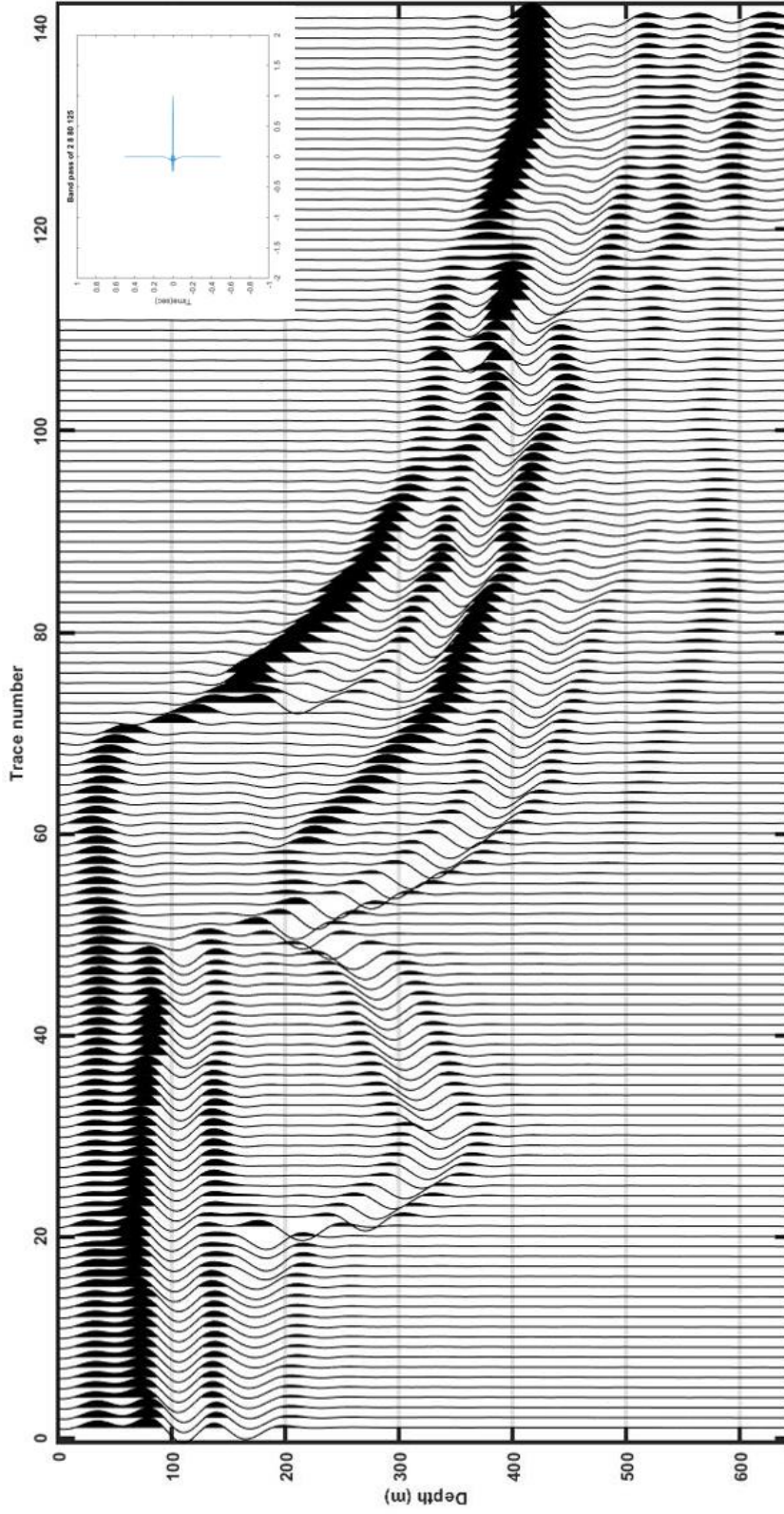
Figure 30: Wiggle plots of model with Ormsby band pass of 2, 8, 80, 125 Hz. Peaks that represents positive amplitude are filled while unfilled troughs represent negative amplitude.
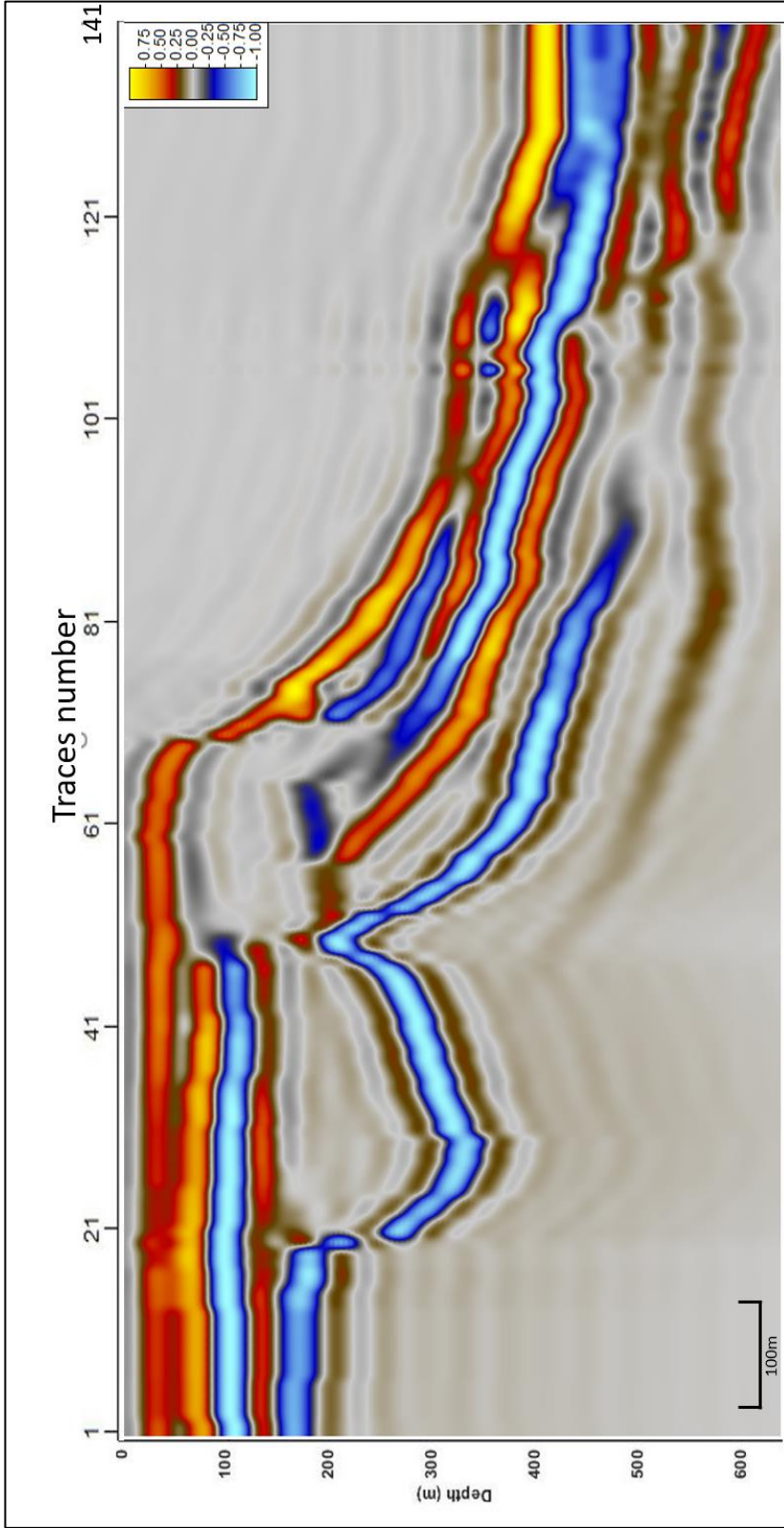
Figure 31: Synthetic seismic profile of the north wall with Ormsby band pass of 2, 8, 80, 125 Hz displayed in Petrel.
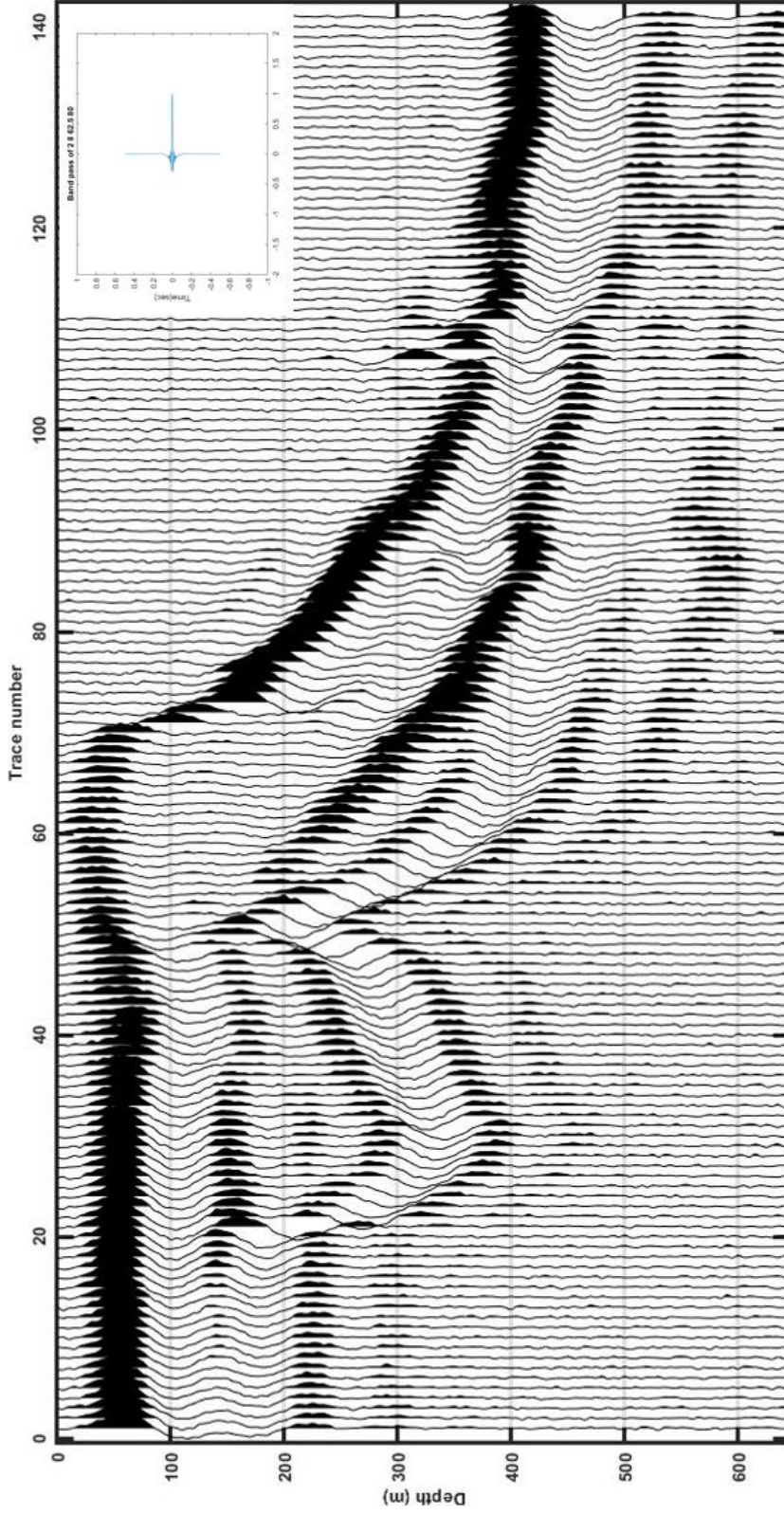
Figure 32: Wiggle plot of model with Ormsby band pass of 2, 8, 62.5, 80 Hz and 5% random noise. Peaks that represents positive amplitude are filled while unfilled troughs represent negative amplitude.
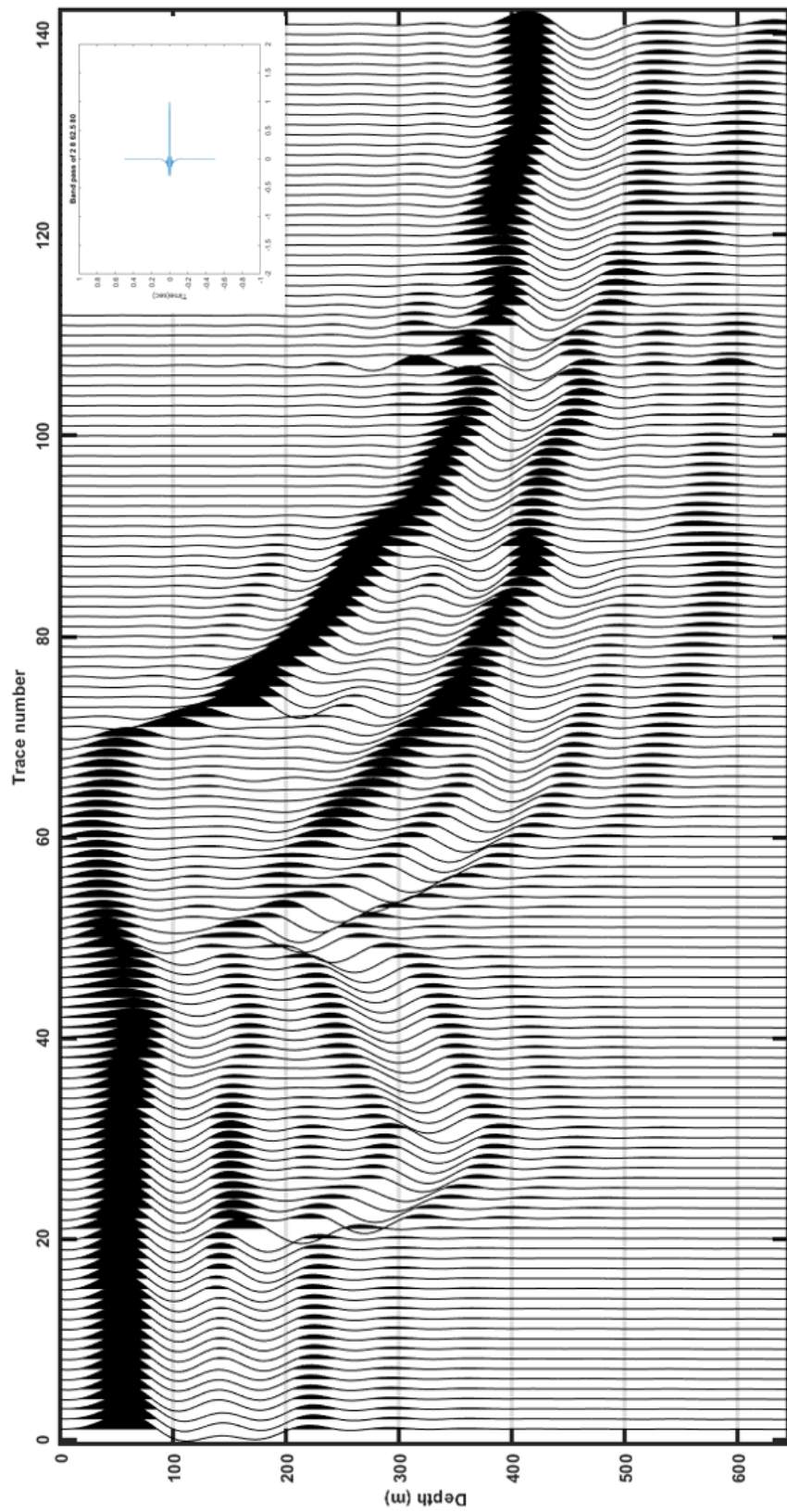
Figure 33: Wiggle plot of model with Ormsby band pass of 2, 8, 62.5, 80 Hz without noise. Peaks that represents positive amplitude are filled while unfilled troughs represent negative amplitude.

Comparation with subsurface data

A comparation is made between the subsurface data from Northwest Shelf margin (Figure 34) and the synthetic seismic data conducted by Omsby wavelet at 2 8 80 125 Hz (Figure 35). Note that the enlarged section of subsurface data exhibits similar features and stratigraphic architecture with synthetic model such as changes of polarity and strength of some reflectors along the slope and reciprocal onlap and downlap of strata on the slope which is expressed by Lamar HFCs in synthetic model.
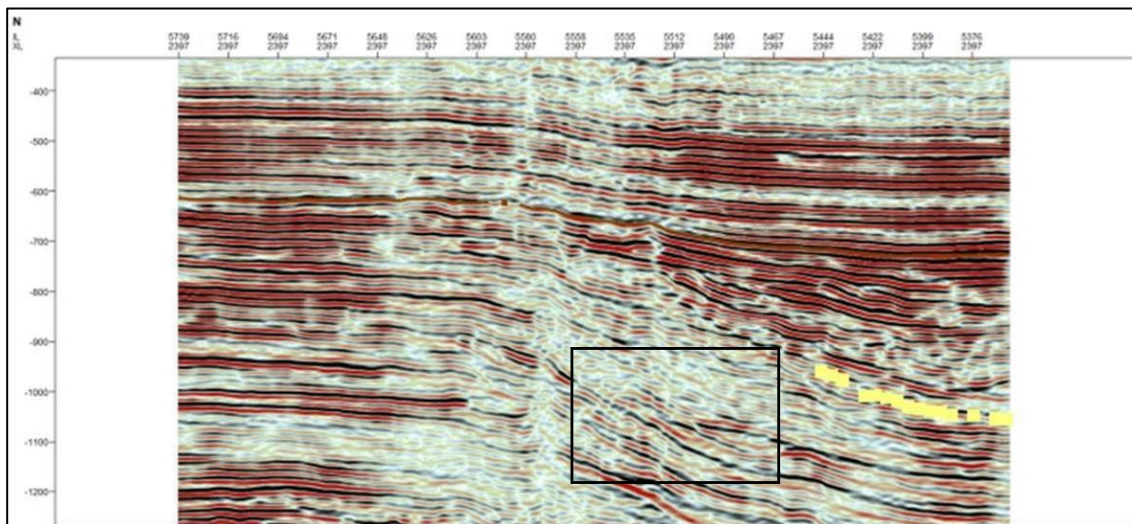
Figure 34: Uninterpreted contemporary 3D seismic line of Guadalupian strata from somewhere on the Northwest Shelf, Permian Basin, New Mexico. Black rectangle is enlarged to compare with synthetic model.
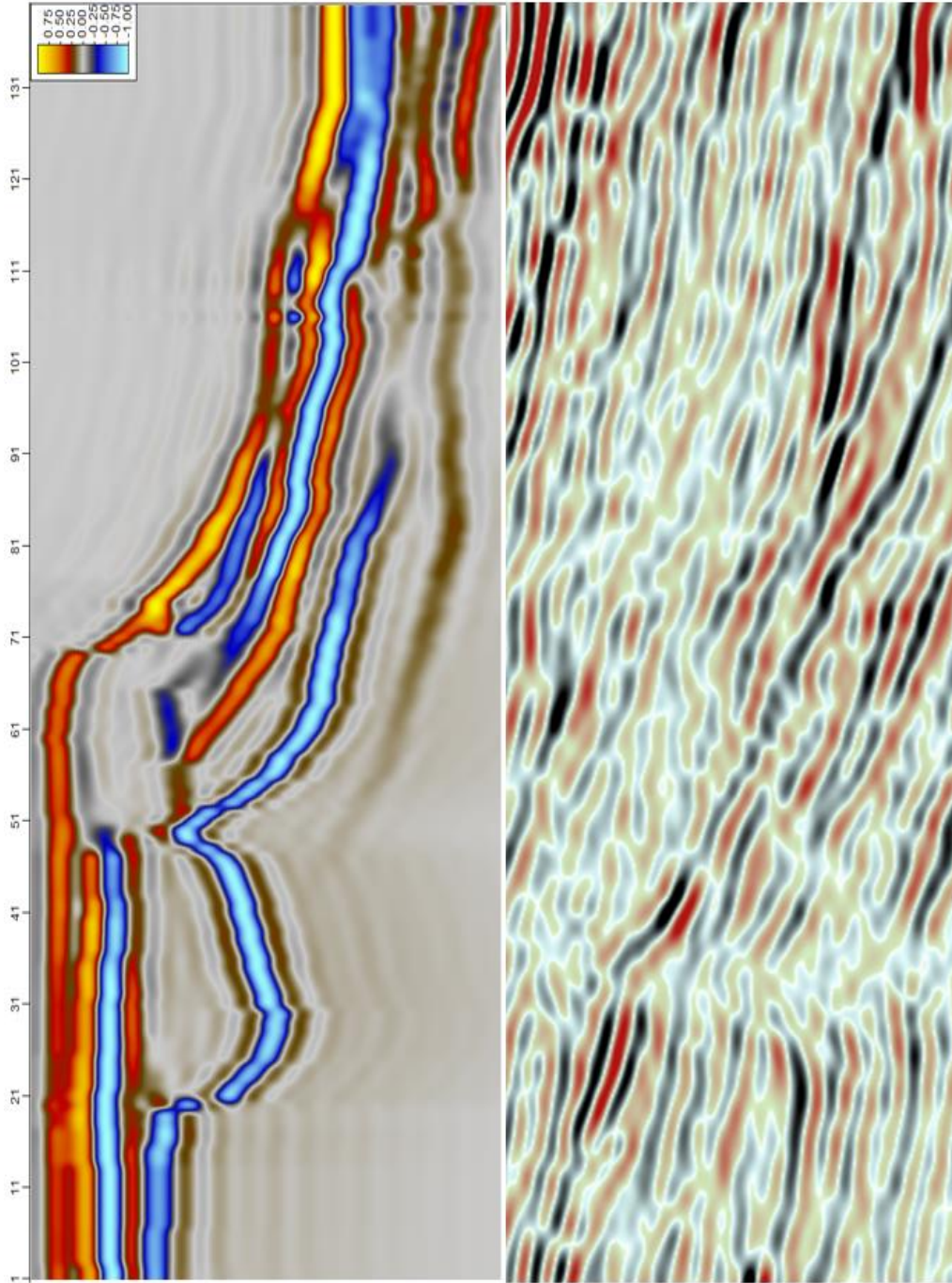
Figure 35: Comparation between the synthetic model and similar section of subsurface seismic data.

CHAPTER 5: CONCLUSIONS

1) The practice of LiDAR employment is valuable for outcrop characterization and interpretation. LiDAR possesses multiple advantages over the traditional photomosaic method as in comparison: 1) the 3D spatial geometry of a target can be better described; 2) the digital nature of the data set allows interpretations to be easily exported to MatLab for further modeling; 3) the high resolution of the data allows strata to be traced across the study area with a higher degree of accuracy.

2) The application of the Schmidt hammer provides an efficient way to estimate P-wave velocity directly from the outcrop. Compared with a lab-based approach, the operation of a Schmidt hammer in the field is simple and non-destructive and allows the computed compressional velocity data of outcrop to be collected from hundreds of locations across a large study area and provides an impedance estimate of heterogeneity.

3) Using the high-resolution point cloud data, detailed stratigraphic architecture is resolved, showing a siliciclastic-carbonate mixing clinoform profile. Specifically the Rader Limestone, McComb Limestone, McKittrick Limestone and Lamar Limestone are found to interfinger three LST sandstone wedges respectively which pinch out on the lower slope, onlapping against underlying carbonate units. The Lamar member is divided into six higher order cycles units where unit 1 and unit 5 are onlapping against unit 2 and unit 4, respectively.

4) Variation of velocity and density occurs not only between different strata, but also within a single stratum. Impedance analysis based on along-slope distance

of strata deposited across the study area indicates that impedance of the Rader member, McComb member and Lamar unit 3 decreases basinward while the Mckittrick Canyon Limestone, Lamar unit 2, 4, and 6 and Reef trail shows an impedance increase basinward.

5) Three Capitan system HFSs of Late Guadalupian documented in the outcrop can be characterized by sequence boundary in the high frequency band pass model and by litho-units in the model with a low frequency band pass wavelet (80 Hz). In the model synthesized with a 2 8 120 250 Hz wavelet, the detailed stratigraphic architectures of Lamar high frequency cycles are well expressed.

6) For this reef-rimmed clinoform profile in outcrop, the identification of surfaces and litho-units in vertical incidence model is greatly influenced by the impedance contrast of upper and lower units and wavelet frequency band pass. Stratigraphic surfaces are better revealed in a high-frequency wavelet modeled seismogram while a mid-to-low frequency band pass produced model characterizes the litho-units.

REFERENCES

Adams, John Emery. "Stratigraphic-tectonic development of Delaware Basin." AAPG Bulletin 49, no. 11 (1965): 2140-2148.

Aydin, A., and A. Basu. "The Schmidt hammer in rock material characterization." Engineering Geology 81, no. 1 (2005): 1-14.

Bakke, Kristina, John Gjelberg, and Steen Agerlin Petersen. "Compound seismic modelling of the Ainsa II turbidite system, Spain: Application to deep-water channel systems offshore Angola." Marine and Petroleum Geology 25, no. 10 (2008): 1058-1073.

Bellian, Jerome A., Charles Kerans, and David C. Jennette. "Digital outcrop models: applications of terrestrial scanning lidar technology in stratigraphic modeling." Journal of sedimentary research 75, no. 2 (2005): 166-176.

Bellian, Jerome A., Charles Kerans, and David C. Jennette. "Digital outcrop models: applications of terrestrial scanning lidar technology in stratigraphic modeling." Journal of sedimentary research 75, no. 2 (2005): 166-176.

Biddle, Kevin T., Wolfgang Schlager, Kurt W. Rudolph, and Terry L. Bush. "Seismic model of a progradational carbonate platform, Picco di Vallandro, the Dolomites, northern Italy (1)." AAPG Bulletin 76, no. 1 (1992): 14-30.

Bosellini, Alfonso. "Progradation geometries of carbonate platforms: examples from the Triassic of the Dolomites, northern Italy." Sedimentology 31, no. 1 (1984): 1-24.

Burton, Darrin, Dallas B. Dunlap, Lesli J. Wood, and Peter P. Flaig. "Lidar intensity as a remote sensor of rock properties." Journal of Sedimentary Research 81, no. 5 (2011): 339-347.

Falivene, O., P. Arbués, J. Ledo, B. Benjumea, J. A. Muñoz, O. Fernández, and S. Martínez. "Synthetic seismic models from outcrop-derived reservoir-scale three-dimensional facies models: The Eocene Ainsa turbidite system (southern Pyrenees)." AAPG bulletin 94, no. 3 (2010): 317-343.

Galley, John E. "Oil and geology in the Permian basin of Texas and New Mexico: North America." (1958): 395-446.

Garber, R. A., P. M. Harris, and J. M. Borer. "Occurrence and Significance of Magnesite in Upper Permian (Guadalupian) Tansill and Yates Formations, Delaware Basin, New Mexico (1)." AAPG Bulletin 74, no. 2 (1990): 119-134.

Garber, Raymond A., George A. Grover, and Paul M. Harris. "Geology of the Capitan shelf margin-subsurface data from the northern Delaware Basin." (1989).

Gardner, G. H. F., L. W. Gardner, and A. R. Gregory. "Formation velocity and density—The diagnostic basics for stratigraphic traps." Geophysics 39, no. 6 (1974): 770-780.

Garrett, Kathryn N., John D. Pigott, and Kulwadee L. Pigott, 2016, High Resolution Basin Modeling Insight Into Syndepositional Permian Reef Architecture Through Integrated Lidar-XRF Analysis, Slaughter Canyon, New Mexico, AAPG Annual Convention and Exhibition, Calgary, Alberta, Canada.

Garrett, Kathryn N., Pigott, John D., and Pigott, Kulwadee L., 2015, High resolution basin modeling of the Permian Capitan reef, New Mexico: new insight from integrated outcrop lidar-xrf-sgr analysis into reef architecture, Geological Society of America Annual Meeting, Baltimore, Maryland, USA , No. 228-401.

Giddens, Emma, John D. Pigott, and Kulwadee L. Pigott. "Pleistocene Coral Reef Destruction in the Florida Keys: Paleotempestite Evidence from a High-Resolution LIDAR XRF Analysis of Windley Key Quarry." Sea 100 (2016): 120.

Hayes, Philip Thayer. Geology of the Guadalupe Mountains, New Mexico. No. 446. US Geological Survey, 1964.

Hayes, Philip Thayer. Geology of the Guadalupe Mountains, New Mexico. No. 446. US Geological Survey, 1964.

Hills, John M. "Sedimentation, tectonism, and hydrocarbon generation in Delaware basin, west Texas and southeastern New Mexico." AAPG Bulletin 68, no. 3 (1984): 250-267.

Horak, R. L. "Tectonic and hydrocarbon maturation history in the Permian Basin." Oil & Gas Journal 83, no. 21 (1985): 124-129.

Janson, X. A. V. I. E. R., S. E. R. G. E. Y. Fomel, O. J. Martinsen, A. J. Pulham, P. D. W. Haughton, and M. D. Sullivan. "3-D forward seismic model of an outcrop-based geocellular model." Concepts in Sedimentology and Paleontology 10 (2011): 87-106.

Katz, O., Z. Reches, and J-C. Roegiers. "Evaluation of mechanical rock properties using a Schmidt Hammer." International Journal of Rock Mechanics and Mining Sciences37, no. 4 (2000): 723-728.

Kenter, J. A. M., GL Bracco Gartner, and W. Schlager. "Seismic models of a mixed carbonate-siliciclastic shelf margin: Permian upper San Andres Formation, Last Chance Canyon, New Mexico." Geophysics 66, no. 6 (2001): 1744-1748.

Kerans, C., P. M. Harris, and D. G. Bebout. "Outer shelf and shelf crest." Guide to the Permian Reef Geology Trail, McKittrick Canyon, Guadalupe Mountains National Park, West Texas: University of Texas, Bureau of Economic Geology, Guidebook 26 (1993): 32-43.

King, Philip Burke. Geology of the southern Guadalupe Mountains, Texas. Vol. 215. US Government Printing Office, 1948.

Lew, C.L., Baharuddin, S.B., and Pigott, John D., 2013, Deepwater Basin Model for the Permian: Delaware Basin Example, China IPTC 16962,17pp.

Miall, Andrew D., and Ronald C. Blakey. "The Phanerozoic tectonic and sedimentary evolution of North America." Sedimentary basins of the world 5 (2008): 1-29.

Newell, Gordon F., and Elliott W. Montroll. "On the theory of the Ising model of ferromagnetism." Reviews of Modern Physics 25, no. 2 (1953): 353.

Osleger, David A., and Scott W. Tinker. "Three-dimensional architecture of Upper Permian high-frequency sequences, Yates-Capitan shelf margin, Permian Basin, USA." (1999).

Palaz, Ibrahim, and Kurt J. Marfurt. "Carbonate seismology: An overview." Carbonate seismology: Society of Exploration Geophysicists Geophysical Developments Series 6 (1997): 1-7.

Pigott, John D., Esra Yalcin, Kulwadee L. Pigott, and Michael Williams, 2015, 3D Delaware basin model: Insight into its heterogeneous petroleum system evolution as a guide to new exploration, West Texas Geological Society Convention, Midland, Tx.

Pigott, John D., Kulwadee L. Pigott, Esra Yalcin, and Michael Williams, 2016, 3D Delaware Basin Petroleum System Evolution: Solution of the Basin Inverse Boundary Value Problem, Hedberg Conference: The Future of Basin and Petroleum Systems Modeling, 3-8 April 2016, Santa Barbara , CA, USA.

Pigott, John D., Michael T. Williams, Mohamed Abdel-Fattah, and Kulwadee L. Pigott, 2014, The Messinian Mediterranean Crisis: A Model for the Permian Delaware Basin? AAPG International Conference & Exhibition, 14-17 September, 2014, Istanbul.

Poole, R. W., and I. W. Farmer. "Consistency and repeatability of Schmidt hammer rebound data during field testing." International Journal of Rock Mechanics and Mining Science17, no. 3 (1980).

Pringle, J. K., J. A. Howell, D. Hodgetts, A. R. Westerman, and D. M. Hodgson. "Virtual outcrop models of petroleum reservoir analogues: a review of the current state-of-the-art." First break 24, no. 3 (2006): 33-42.

Read, J. F. "Overview of carbonate platform sequences, cycle stratigraphy and reservoirs in greenhouse and icehouse worlds." (1995).

Rush, Jason, and Charles Kerans. "Stratigraphic response across a structurally dynamic shelf: the latest Guadalupian composite sequence at Walnut Canyon, New Mexico, USA." Journal of Sedimentary Research 80, no. 9 (2010): 808-828.

Saller, Arthur H., J. A. D. Dickson, and Fumiaki Matsuda. "Evolution and distribution of porosity associated with subaerial exposure in upper Paleozoic platform limestones, west Texas." AAPG bulletin 83, no. 11 (1999): 1835-1854.

Saller, Arthur H., Paul M. Mitch Harris, Brenda L. Kirkland, and S. J. Mazzullo. "Geologic Framework of the Capitan Depositional System Previous Studies, Controversies, and Contents of this Special Publication." (1999).

Sarg, J. F. "Foredeep: Middle-Late Permian Depositional Sequences, Permian Basin, West Texas and New Mexico." (1987): 140-154.

Schwab, A. M., B. T. Cronin, and H. Ferreira. "Seismic expression of channel outcrops: Offset stacked versus amalgamated channel systems." Marine and Petroleum Geology 24, no. 6-9 (2007): 504-514.

Sharma, P. K., Manoj Khandelwal, and T. N. Singh. "A correlation between Schmidt hammer rebound numbers with impact strength index, slake durability index and P-wave velocity." International Journal of Earth Sciences 100, no. 1 (2011): 189-195.

Stafleu, Jan, and Mark D. Sonnenfeld. "Seismic models of a shelf-margin depositional sequence: upper San Andres formation, Last Chance Canyon, New Mexico." Journal of Sedimentary Research 64, no. 4 (1994).

Sullivan, Morgan, Gerrick Jensen, Frank Goulding, David Jennette, Lincoln Foreman, and David Stern. "Architectural analysis of deep-water outcrops: Implications for exploration and development of the Diana sub-basin, western Gulf of Mexico." In Deep-water reservoirs of the world: Gulf Coast Section SEPM Foundation 20th Annual Research Conference, pp. 1010-1032. 2000.

Tinker, Scott W. "Shelf-to-basin facies distributions and sequence stratigraphy of a steep-rimmed carbonate margin: Capitan depositional system, McKittrick Canyon, New Mexico and Texas." Journal of Sedimentary Research 68, no. 6 (1998).

Tinker, Scott Wheeler. "Reservoir-scale sequence stratigraphy: McKittrick Canyon, and three-dimensional subsurface examples, west Texas and New Mexico." (1997): 6141-6141.

Ward, Robert F., Christopher G. St C. Kendall, and Paul M. Harris. "Upper Permian (Guadalupian) facies and their association with hydrocarbons--Permian basin, west Texas and New Mexico." AAPG Bulletin 70, no. 3 (1986): 239-262.

Ward, Robert F., Christopher G. St C. Kendall, and Paul M. Harris. "Upper Permian (Guadalupian) facies and their association with hydrocarbons--Permian basin, west Texas and New Mexico." AAPG Bulletin 70, no. 3 (1986): 239-262.

Wehr, Aloysius, and Uwe Lohr. "Airborne laser scanning—an introduction and overview." ISPRS Journal of photogrammetry and remote sensing 54, no. 2-3 (1999): 68-82.

Williams, Michael T., John D. Pigott, and Kulwadee L. Pigott, 2014, Delaware Basin Evolution: Preliminary Integrated 1D,2D, And 3D Basin Model for Petroleum System Analysis, 2014, AAPG Annual Convention & Exhibition, Houston, Tx.

Williams, Michael Thomas. "Evolution of the Delaware Basin, West Texas and Southeast New Mexico." PhD diss., University of Oklahoma, 2013.

Winkler, Stefan, and John A. Matthews. "Comparison of electronic and mechanical Schmidt hammers in the context of exposure-age dating: are Q-and R-values interconvertible?." Earth Surface Processes and Landforms 39, no. 8 (2014): 1128-1136.

Yagiz, Saffet. "Predicting uniaxial compressive strength, modulus of elasticity and index properties of rocks using the Schmidt hammer." Bulletin of Engineering Geology and the Environment 68, no. 1 (2009): 55-63.

Yang, Kenn-Ming, and Stephen L. Dorobek. "The Permian basin of west Texas and New Mexico: tectonic history of a" composite" foreland basin and its effects on stratigraphic development." Stratigraphic evolution of foreland basins: SEPM Special Publication 52 (1995): 149-174.

Yang, Kenn-Ming, and Stephen L. Dorobek. "The Permian basin of west Texas and New Mexico: tectonic history of a" composite" foreland basin and its effects on stratigraphic development." Stratigraphic evolution of foreland basins: SEPM Special Publication 52 (1995): 149-174.

APPENDICES

Appendix I—Data set of Schmidt hammer readings and rock samples

Sample	GPS(Long)	GPS(Lat)	Q	R	Vp (m/s)	Density (g/cm^3)	AI (kg·m^-2·s^-1·10^6)
South1	-104.758148	31.97992215	62.8	54.18046	3995.5	2.72	10.868
South2	-104.7579382	31.97943538	69.3	60.79876	4752	2.69	12.783
South3	-104.7579382	31.97943538	68.1	59.57692	4602.3	2.68	12.334
South4	-104.7579382	31.97943538	69.4	60.90058	4764.7	2.7	12.865
South5			69.5	61.0024	4777.4		
South6	-104.7579382	31.97943538	59.7	51.02404	3678.4	2.52	9.269
South7	-104.7605925	31.98196064	69.5	61.0024	4777.4	2.46	11.752
South8	-104.7568244	31.97983549	73	64.5661	5245	2.43	12.745
South9	-104.7567332	31.97985918	71.3	62.83516	5012.4	2.69	13.483
South10	-104.7605925	31.98196064	62.4	53.77318	3953.1	2.62	10.357
South11	-104.7567332	31.97985918	68.8	60.28966	4689	2.35	11.019
South12	-104.7605925	31.98196064	65	56.4205	4237	2.51	10.635
South13	-104.7598914	31.98269146	68	59.4751	4590	2.65	12.164
South14	-104.7598914	31.98269146	65.7	57.13324	4316.9	2.65	11.44
South15	-104.7598914	31.98269146	69.4	60.90058	4764.7	2.67	12.722
South16	-104.7598914	31.98269146	67.2	58.66054	4493.1	2.74	12.311
South17			78	69.6571	5993.4		
South18	-104.7613056	31.98733333	58.2	49.49674	3534.1	2.677	9.462
South19	-104.7615278	31.98713889	62.3	53.67136	3942.5	2.659	10.482
South20	-104.7614722	31.98705556	61.2	52.55134	3828.5	2.659	10.179
South21	-104.7616389	31.98672222	64.2	55.60594	4147.5	2.617	10.855

South22	-104.7616944	31.9865	66.5	57.9478	4410	2.721	12
South23	-104.7616389	31.98652778	61.9	53.26408	3900.7	2.639	10.295
South24	-104.76175	31.98625	58.6	49.90402	3572	2.703	9.654
South25	-104.7617222	31.98597222	62.2	53.56954	3932		
South26	-104.7618333	31.98552778	66.1	57.54052	4363.2	2.674	11.665
South27	-104.7620556	31.98558333	58.2	49.49674	3534.1	2.708	9.57
South28	-104.7624167	31.98530556	56.1	47.35852	3341.5	2.728	9.114
South29	-104.7626944	31.98477778	68.9	60.39148	4701.6	2.679	12.594
South30	-104.7627778	31.98430556	66	57.4387	4351.5	2.671	11.622
South31	-104.7629167	31.98352778	64.6	56.01322	4192	2.657	11.138
South32	-104.7630278	31.98333333	63.6	54.99502	4081.7	2.753	11.236
South33	-104.7632222	31.98291667	65.9	57.33688	4339.9	2.657	11.531
South34	-104.7633889	31.98258333	63.5	54.8932	4070.8		
South35	-104.7634167	31.98197222	72.7	64.26064	5203.2	2.578	13.411
South36	-104.7636111	31.98175	64.4	55.80958	4169.7	2.714	11.317
South37	-104.7637778	31.98075	63	54.3841	4016.9	2.686	10.788
Trail2	-104.7560359	31.98575355	76.9	68.53708	5820	2.692	15.666
Trail3	-104.7560359	31.98575355	66.3	57.74416	4386.5	2.633	11.548

Trail4	-104.754562	31.98493208	61.3	52.65316	3838.8	2.658	10.202
Trail5	-104.7551478	31.98498368	66.6	58.04962	4421.8	2.678	11.843
Trail6	-104.7558083	31.98505578	74.4	65.99158	5444.6	2.667	14.521
Trail7	-104.7558436	31.98643666	70.2	61.71514	4867.5	2.697	13.129
Trail7-1	-104.7564598	31.98543956	71.5	63.0388	5039.2	2.693	13.572
Trail7-2	-104.7564072	31.98542501	76.7	68.33344	5789.1	2.714	15.709
Trail7-3	-104.7563545	31.98540664	77.2	68.84254	5866.8	2.704	15.866
Trail7-4	-104.7562904	31.98539743	73.1	64.66792	5259	2.669	14.038
Trail7-5	-104.7562339	31.98540658	66.3	57.74416	4386.5	2.628	11.528
Trail7-6	-104.7561432	31.98541676	67.9	59.37328	4577.8	2.651	12.137
Trail7-7	-104.7560612	31.98542592	69.6	61.10422	4790.2	2.595	12.43
Trail8	-104.7559888	31.98542457	68.1	59.57692	4602.3	2.667	12.272
Trail8-2	-104.7557288	31.98543624	64.8	56.21686	4214.4	2.592	10.923
Trail8-3	-104.7556545	31.98556271	63.6	54.99502	4081.7	2.572	10.497
Trail8-4	-104.7559589	31.98569158	68	59.4751	4590	2.457	11.277
Trail8-5	-104.7561327	31.98580998	66.8	58.25326	4445.4	2.658	11.817
Trail8-6	-104.7562062	31.9864406	61.3	52.65316	3838.8	2.733	10.492
Trail8-7	-104.7562128	31.98672086	64.2	55.60594	4147.5	2.666	11.056
Trail8-8	-104.7561065	31.98708957	56	47.2567	3332.6	2.635	8.782
Trail8-9	-104.7559876	31.98740039	62.8	54.18046	3995.5	2.636	10.534
Trail8-11	-104.7559439	31.98767277	59.4	50.71858	3649	2.58	9.415
Trail8-12	-104.7559756	31.98786794	72.8	64.36246	5217.1	2.657	13.861
Trail8-13	-104.7559908	31.98809665	60.9	52.24588	3798	2.542	9.656

Trail8-14	-104.7560633	31.98830653	56.1	47.35852	3341.5	2.68	8.956
Trail9	-104.756198	31.988753	67.4	58.86418	4517.1	2.556	11.544
Trail9-1	-104.756864	31.989405	72.1	63.64972	5120.5		0
Trail9-2	-104.7565883	31.98902524	68.2	59.67874	4614.6	2.658	12.263
Trail10	-104.757025	31.989685	71.6	63.14062	5052.7	2.637	13.326
Trail10-1	-104.7571046	31.99011368		-9.7625	748.2	2.72	2.035
Trail11	-104.757309	31.990556	63.8	55.19866	4103.5	2.642	10.84
Trail12	-104.757691	31.991591	60.3	51.63496	3737.7	2.762	10.323
Trail13	-104.758637	31.99268594	69.1	60.59512	4726.7	2.705	12.786
Trail13-1	-104.7603857	31.99322884	63.3	54.68956	4049.1	2.45	9.921
Trail14	-104.7614724	31.99388699	74.2	65.78794	5415.6	2.63	14.245
Trail15	-104.7573703	31.99376086	72.7	64.26064	5203.2	2.535	13.189
Trail16	-104.7572079	31.99410389	67.2	58.66054	4493.1	2.63	11.815
Trail17	-104.7574491	31.99449904	62.2	53.56954	3932	2.669	10.493
Trail18	-104.758523	31.995345	67.6	59.06782	4541.3	2.665	12.1
Trail18-1	-104.758247	31.994467	66.5	57.9478	4410	2.703	11.92
Trail19	-104.7589204	31.99543965	69.6	61.10422	4790.2	2.695	12.91
Trail20	-104.7585104	31.99587395	67.4	58.86418	4517.1	2.568	11.598
Trail21	-104.757303	31.997653	68.4	59.88238	4639.3	2.702	12.535
Trail22	-104.7559254	31.99800061	67.3	58.76236	4505.1	2.725	12.275
Trail23	-104.7557524	31.99800756	64.5	55.9114	4180.9	2.658	11.114
Trail24	-104.7558722	31.99812352	65.1	56.52232	4248.3	2.696	11.454

Trail25	-104.7567737	31.9983872	67	58.4569	4469.2	2.624	11.728
Trail26	-104.7587606	31.99803498	72.7	64.26064	5203.2	2.606	13.558
Trail26-1	-104.7594411	31.9978911	70.3	61.81696	4880.5	2.427	11.842
Trail26-3	-104.7588914	31.9978801	68.9	60.39148	4701.6	2.472	11.62
Trail27	-104.7598195	31.99766476	70.3	61.81696	4880.5	2.649	12.93
Trail27-2	-104.7595383	31.99810126	73.3	64.87156	5287.1	2.641	13.963
Trail27-3	-104.7598789	31.99774537	66.6	58.04962	4421.8	2.698	11.931
Trail28	-104.7593804	31.99828032	70.9	62.42788	4959.2	2.657	13.176
NSlope1	-104.75862	31.984437	52.4	43.59118	3027.5	2.65	8.023
NSlope2	-104.758594	31.984442	63.1	54.48592	4027.6	2.695	10.856
NSlope3	-104.758584	31.984441	62.3	53.67136	3942.5	2.719	10.718
NSlope4	-104.758281	31.984754	65.7	57.13324	4316.9	2.664	11.502
NSlope5	-104.758006	31.98542	61.7	53.06044	3879.9	2.457	9.534
NSlope6	-104.758028	31.985744	65	56.4205	4237	2.718	11.516
NSlope7	-104.757979	31.985953	60.6	51.94042	3767.7	2.517	9.483
NSlope8	-104.757838	31.986357	68.2	59.67874	4614.6	2.613	12.056
NSlope9	-104.757937	31.986694	60.4	51.73678	3747.7	2.624	9.832
NSlope10	-104.7577	31.986583	66	57.4387	4351.5	2.704	11.766
NSlope11	-104.757433	31.986634	69.2	60.69694	4739.3	2.549	12.082
NSlope12	-104.757377	31.986638	61.5	52.8568	3859.3	2.441	9.421
NSlope13	-104.757321	31.986617	31.6	22.41262	1738.2	2.408	4.185
NSlope14	-104.757141	31.986249	36.3	27.19816	1970.4	2.504	4.933
NSlope15	-104.757044	31.986264	65.7	57.13324	4316.9	2.504	10.807
NSlope16	-104.756914	31.986247	39	29.9473	2117.5	2.733	5.786

NSlope17	-104.756819	31.986179	63.8	55.19866	4103.5		2.651	10.879
NSlope18	-104.756747	31.986176	55.6	46.84942	3297.3		2.712	8.942
NSlope19	-104.756494	31.986201	56.5	47.7658	3377.4		2.705	9.136
NSlope20	-104.756428	31.986187	27.1	17.83072	1541.6		2.511	3.87
NSlope21	-104.75714	31.986039	60.5	51.8386	3757.7		2.501	9.397
NSlope22	-104.756587	31.985764	56.4	47.66398	3368.4		2.708	9.122
NSlope23	-104.756673	31.985425	53.6	44.81302	3125.9		2.658	8.309
NSlope24	-104.756688	31.985205	29.1	19.86712	1626.1		2.682	4.361
NSlope25	-104.756574	31.984926	48.3	39.41656	2713.8		2.633	7.144
NSlope26	-104.756719	31.984773	58.1	49.39492	3524.7		2.604	9.178
NSlope27	-104.756956	31.984568	42.8	33.81646	2343.5		2.29	5.365
NSlope28	-104.757117	31.984456	60.5	51.8386	3757.7		2.378	8.936
NSlope29	-104.757072	31.984429	62.3	53.67136	3942.5		2.671	10.532
NSlope30	-104.757343	31.984226	63.8	55.19866	4103.5		2.752	11.293
NSlope31	-104.757343	31.984226	49	40.1293	2765		2.746	7.594
NSlope32	-104.757483	31.984144	42.9	33.91828	2349.7		2.386	5.606
NSlope33	-104.757772	31.983897	69	60.4933	4714.1		2.605	12.278

Appendix II—Matlab Code for AI and Seismic Modeling

This chapter is including the code for editing of stratigraphy frame exported from Riscan Pro and impedance model building.

Example of stratigraphic surface extraction with coordinate rotation

```matlab
% Surface location read out from polygon dxf file
exported from LiDAR
%
% Written by Zhuobo Wang Dec 2017
% Input
%     N_Lamar1.xlsx etc. : xlsx file of base of unit
Lamar1 transfered from
%                          original dxf file
%     RotM1/RotM2: Rotation matrix which rotate the
coordinated of node in
%                  surface to desired coordinate
system (consistent with stratigraphy frame)
%Output
%     Lamar1_x/Lamar1_z: Rotated coordinate of node on
Lamar1 surface


% read out the coordinate of surface polygon
[num,txt,raw]=xlsread('N_Lamar1.xlsx');

C=num;
m=1;
for n=1:length(C)
    if C(n)==10
    Lamar1(1,m)=C(n+1);
    Lamar1(2,m)=C(n+3);
    Lamar1(3,m)=C(n+5);
    m=m+1;
    end
end

RotM1=[cos(pi/6),0,-
sin(pi/6);0,1,0;sin(pi/6),0,cos(pi/6)];
```

```matlab
RotM2=[1,0,0;0,cos(pi/12),sin(pi/12);0,-
sin(pi/12),cos(pi/12)];


Lamar1_tran=RotM1*Lamar1;
Lamar1_tran=RotM2*Lamar1_tran;



Lamar1_x=Lamar1_tran(1,:);
Lamar1_y=Lamar1_tran(2,:);
Lamar1_z=Lamar1_tran(3,:);
% stratigraphy adjustment and plot
Lamar1_x(1)=[];
Lamar1_y(1)=[];
Lamar1_z(1)=[];
Lamar1_x=Lamar1_x-1100;
Lamar1_z=Lamar1_z-100;
Lamar1_x=-Lamar1_x;
plot(Lamar1_x,Lamar1_z,'*');
```

Impedance model building and reflection coefficient arrays generation

```matlab
% Impedance Model for McKittrick Canyon north wall
% Based on stacking pattern, assign AI to every sample to every
traces.
%
% Written by: Zhuobo Wang Dec 2017
% Input
%     Min_x/Max_x: range of traces location at horizontal
direction
%     Trace_inter: interval of traces placing
%     PostLamar_x/PostLamar_z ect. : horizontal and vertical
coordinate of base of PostLamar unit
%     Imp_Postlamar ect. : Acoustic Impedance array of unit
%     i: traces number
%     nsamp: number of sample in every trace
% Output
%     Z1: Acoustic Impedance matrix of study area
%     RC_M1: Reflection coefficient matrix of all traces
Min_x=600;
Max_x=800;
Trace_inter=10;
Hori=[-600:10:800];
nsamp=131;
for i=1:16 % assign impedance to trace 1-16 where stacking
pattern is same
```

```matlab
        SurLoc=[0,0,0,0];
        % calculate location of stratigraphy surfaces which
represent
        % surface of impedance change
        SurLoc(1)=nsamp-
fix((interp1(PostLamar_x,PostLamar_z,Hori(i),'liner','extrap'))/
5);
        SurLoc(2)=nsamp-
fix((interp1(Lamar2B_x,Lamar2B_z,Hori(i),'liner','extrap'))/5);
        SurLoc(3)=nsamp-
fix((interp1(SandB_x,SandB_z,Hori(i),'liner','extrap'))/5);
        SurLoc(4)=nsamp-
fix((interp1(Mck_x,Mck_z,Hori(i),'liner','extrap'))/5);

        for j=1:SurLoc(1)
            Z1(j,i)=11;
        end
        for j=SurLoc(1)+1:SurLoc(2)
            Z1(j,i)=Imp_Tansil(i);
        end
        for j=SurLoc(2)+1:SurLoc(3)
            Z1(j,i)=Imp_Yates6(i);
        end
        for j=SurLoc(3)+1:SurLoc(4)
            Z1(j,i)=Imp_Yates5(i);
        end
        for j=SurLoc(4)+1:nsamp
            Z1(j,i)=Imp_Mc(i);
        end


end
for i=17:31

        SurLoc=[0,0,0,0,0];
        SurLoc(1)=nsamp-
fix((interp1(PostLamar_x,PostLamar_z,Hori(i),'liner','extrap'))/
5);
        SurLoc(2)=nsamp-
fix((interp1(Lamar2B_x,Lamar2B_z,Hori(i),'liner','extrap'))/5);
        SurLoc(3)=nsamp-
fix((interp1(SandB_x,SandB_z,Hori(i),'liner','extrap'))/5);
        SurLoc(4)=nsamp-
fix((interp1(ReefT_x,ReefT_z,Hori(i),'liner','extrap'))/5);
        SurLoc(5)=nsamp-
fix((interp1(Mck_x,Mck_z,Hori(i),'liner','extrap'))/5);

        for j=1:SurLoc(1)
            Z1(j,i)=11;
        end
        for j=SurLoc(1)+1:SurLoc(2)
```

```matlab
            Z1(j,i)=Imp_Tansil(i);
        end
        for j=SurLoc(2)+1:SurLoc(3)
            Z1(j,i)=Imp_Yates6(i);
        end
        for j=SurLoc(3)+1:SurLoc(4)
            Z1(j,i)=Imp_Yates5(i);
        end
        for j=SurLoc(4)+1:SurLoc(5)
            Z1(j,i)=Imp_Reef(i);
        end
        for j=SurLoc(5)+1:nsamp
            Z1(j,i)=Imp_Mc(i);
        end
end

for i=32:41

        SurLoc=[0,0,0,0,0,0];
        SurLoc(1)=nsamp-
fix((interp1(PostLamar_x,PostLamar_z,Hori(i),'liner','extrap'))/
5);
        SurLoc(2)=nsamp-
fix((interp1(Lamar2B_x,Lamar2B_z,Hori(i),'liner','extrap'))/5);
        SurLoc(3)=nsamp-
fix((interp1(SandB_x,SandB_z,Hori(i),'liner','extrap'))/5);
        SurLoc(4)=nsamp-
fix((interp1(ReefT_x,ReefT_z,Hori(i),'liner','extrap'))/5);
        SurLoc(5)=nsamp-
fix((interp1(ReefB_x,ReefB_z,Hori(i),'liner','extrap'))/5);
        SurLoc(6)=nsamp-
fix((interp1(Mck_x,Mck_z,Hori(i),'liner','extrap'))/5);

        for j=1:SurLoc(1)
            Z1(j,i)=11;
        end
        for j=SurLoc(1)+1:SurLoc(2)
            Z1(j,i)=Imp_Tansil(i);
        end
        for j=SurLoc(2)+1:SurLoc(3)
            Z1(j,i)=Imp_Yates6(i);
        end
        for j=SurLoc(3)+1:SurLoc(4)
            Z1(j,i)=Imp_Yates5(i);
        end
        for j=SurLoc(4)+1:SurLoc(5)
            Z1(j,i)=Imp_Reef(i);
        end
        for j=SurLoc(5)+1:SurLoc(6)
            Z1(j,i)=Imp_Mck(i);
        end
```

```matlab
        for j=SurLoc(6)+1:nsamp
            Z1(j,i)=Imp_Mc(i);
        end


end

for i=42:51

        SurLoc=[0,0,0,0,0,0,0];
        SurLoc(1)=nsamp-
fix((interp1(PostLamar_x,PostLamar_z,Hori(i),'liner','extrap'))/
5);
        SurLoc(2)=nsamp-
fix((interp1(Lamar2B_x,Lamar2B_z,Hori(i),'liner','extrap'))/5);
        SurLoc(3)=nsamp-
fix((interp1(ReefT_x,ReefT_z,Hori(i),'liner','extrap'))/5);
        SurLoc(4)=nsamp-
fix((interp1(SandB_x,SandB_z,Hori(i),'liner','extrap'))/5);
        SurLoc(5)=nsamp-
fix((interp1(ReefB_x,ReefB_z,Hori(i),'liner','extrap'))/5);
        SurLoc(6)=nsamp-
fix((interp1(Mck_x,Mck_z,Hori(i),'liner','extrap'))/5);

        for j=1:SurLoc(1)
            Z1(j,i)=11;
        end
        for j=SurLoc(1)+1:SurLoc(2)
            Z1(j,i)=Imp_Tansil(i);
        end
        for j=SurLoc(2)+1:SurLoc(3)
            Z1(j,i)=Imp_Yates6(i);
        end
        for j=SurLoc(3)+1:SurLoc(4)
            Z1(j,i)=Imp_Yates5(i);
        end
        for j=SurLoc(4)+1:SurLoc(5)
            Z1(j,i)=Imp_Reef(i);
        end
        for j=SurLoc(5)+1:SurLoc(6)
            Z1(j,i)=Imp_Mck(i);
        end
        for j=SurLoc(6)+1:nsamp
            Z1(j,i)=Imp_Mc(i);
        end



end
```

```matlab
for i=52:58

        SurLoc=[0,0,0,0,0,0,0];
        SurLoc(1)=nsamp-
fix((interp1(PostLamar_x,PostLamar_z,Hori(i),'liner','extrap'))/
5);
        SurLoc(2)=nsamp-
fix((interp1(ReefT_x,ReefT_z,Hori(i),'liner','extrap'))/5);
        SurLoc(3)=nsamp-
fix((interp1(ReefB_x,ReefB_z,Hori(i),'liner','extrap'))/5);
        SurLoc(4)=nsamp-
fix((interp1(SandB_x,SandB_z,Hori(i),'liner','extrap'))/5);
        SurLoc(5)=nsamp-
fix((interp1(Mck_x,Mck_z,Hori(i),'liner','extrap'))/5);

        for j=1:SurLoc(1)
            Z1(j,i)=11;
        end
        for j=SurLoc(1)+1:SurLoc(2)
            Z1(j,i)=Imp_Tansil(i);
        end
        for j=SurLoc(2)+1:SurLoc(3)
            Z1(j,i)=Imp_Reef(i);
        end
        for j=SurLoc(3)+1:SurLoc(4)
            Z1(j,i)=Imp_Unk(i);
        end
        for j=SurLoc(4)+1:SurLoc(5)
            Z1(j,i)=Imp_Mck(i);
        end
        for j=SurLoc(5)+1:nsamp
            Z1(j,i)=Imp_Mc(i);
        end




end

for i=59:63

        SurLoc=[0,0,0,0,0,0,0];
        SurLoc(1)=nsamp-
fix((interp1(PostLamar_x,PostLamar_z,Hori(i),'liner','extrap'))/
5);
        SurLoc(2)=nsamp-
fix((interp1(ReefT_x,ReefT_z,Hori(i),'liner','extrap'))/5);
        SurLoc(3)=nsamp-
fix((interp1(ReefB_x,ReefB_z,Hori(i),'liner','extrap'))/5);
```

```matlab
        SurLoc(4)=nsamp-
fix((interp1(Lamar2B_x,Lamar2B_z,Hori(i),'liner','extrap'))/5);
        SurLoc(5)=nsamp-
fix((interp1(SandB_x,SandB_z,Hori(i),'liner','extrap'))/5);
        SurLoc(6)=nsamp-
fix((interp1(Mck_x,Mck_z,Hori(i),'liner','extrap'))/5);

        for j=1:SurLoc(1)
            Z1(j,i)=11;
        end
        for j=SurLoc(1)+1:SurLoc(2)
            Z1(j,i)=Imp_Tansil(i);
        end
        for j=SurLoc(2)+1:SurLoc(3)
            Z1(j,i)=Imp_Reef(i);
        end
        for j=SurLoc(3)+1:SurLoc(4)
            Z1(j,i)=Imp_Lamar2(i);
        end
        for j=SurLoc(4)+1:SurLoc(5)
            Z1(j,i)=Imp_Unk(i);
        end
        for j=SurLoc(5)+1:SurLoc(6)
            Z1(j,i)=Imp_Mck(i);
        end
        for j=SurLoc(6)+1:nsamp
            Z1(j,i)=Imp_Mc(i);
        end




end

for i=64:66

        SurLoc=[0,0,0,0,0,0,0,0];
        SurLoc(1)=nsamp-
fix((interp1(PostLamar_x,PostLamar_z,Hori(i),'liner','extrap'))/
5);
        SurLoc(2)=nsamp-
fix((interp1(ReefT_x,ReefT_z,Hori(i),'liner','extrap'))/5);
        SurLoc(3)=nsamp-
fix((interp1(ReefB_x,ReefB_z,Hori(i),'liner','extrap'))/5);
        SurLoc(4)=nsamp-
fix((interp1(Lamar2_x,Lamar2_z,Hori(i),'liner','extrap'))/5);
        SurLoc(5)=nsamp-
fix((interp1(Lamar2B_x,Lamar2B_z,Hori(i),'liner','extrap'))/5);
```

```matlab
        SurLoc(6)=nsamp-
fix((interp1(SandB_x,SandB_z,Hori(i),'liner','extrap'))/5);
        SurLoc(7)=nsamp-
fix((interp1(Mck_x,Mck_z,Hori(i),'liner','extrap'))/5);

        for j=1:SurLoc(1)
            Z1(j,i)=11;
        end
        for j=SurLoc(1)+1:SurLoc(2)
            Z1(j,i)=Imp_Tansil(i);
        end
        for j=SurLoc(2)+1:SurLoc(3)
            Z1(j,i)=Imp_Reef(i);
        end
        for j=SurLoc(3)+1:SurLoc(4)
            Z1(j,i)=Imp_Lamar3(i);
        end
        for j=SurLoc(4)+1:SurLoc(5)
            Z1(j,i)=Imp_Lamar2(i);
        end
        for j=SurLoc(5)+1:SurLoc(6)
            Z1(j,i)=Imp_Unk(i);
        end
        for j=SurLoc(6)+1:SurLoc(7)
            Z1(j,i)=Imp_Mck(i);
        end
        for j=SurLoc(7)+1:nsamp
            Z1(j,i)=Imp_Mc(i);
        end
end

for i=67:72

        SurLoc=[0,0,0,0,0,0,0,0];
        SurLoc(1)=nsamp-
fix((interp1(PostLamar_x,PostLamar_z,Hori(i),'liner','extrap'))/
5);
        SurLoc(2)=nsamp-
fix((interp1(ReefB_x,ReefB_z,Hori(i),'liner','extrap'))/5);
        SurLoc(3)=nsamp-
fix((interp1(Lamar4_x,Lamar4_z,Hori(i),'liner','extrap'))/5);
        SurLoc(4)=nsamp-
fix((interp1(Lamar2_x,Lamar2_z,Hori(i),'liner','extrap'))/5);
        SurLoc(5)=nsamp-
fix((interp1(Lamar2B_x,Lamar2B_z,Hori(i),'liner','extrap'))/5);
        SurLoc(6)=nsamp-
fix((interp1(SandB_x,SandB_z,Hori(i),'liner','extrap'))/5);
        SurLoc(7)=nsamp-
fix((interp1(Mck_x,Mck_z,Hori(i),'liner','extrap'))/5);

        for j=1:SurLoc(1)
```

```matlab
                Z1(j,i)=11;
          end
          for j=SurLoc(1)+1:SurLoc(2)
                Z1(j,i)=Imp_Reef(i);
          end
          for j=SurLoc(2)+1:SurLoc(3)
                Z1(j,i)=Imp_Lamar4(i);
          end
          for j=SurLoc(3)+1:SurLoc(4)
                Z1(j,i)=Imp_Lamar3(i);
          end
          for j=SurLoc(4)+1:SurLoc(5)
                Z1(j,i)=Imp_Lamar2(i);
          end
          for j=SurLoc(5)+1:SurLoc(6)
                Z1(j,i)=Imp_Unk(i);
          end
          for j=SurLoc(6)+1:SurLoc(7)
                Z1(j,i)=Imp_Mck(i);
          end
          for j=SurLoc(7)+1:nsamp
                Z1(j,i)=Imp_Mc(i);
          end
end

for i=73:78


          SurLoc=[0,0,0,0,0,0,0,0];
          SurLoc(1)=nsamp-
fix((interp1(PostLamar_x,PostLamar_z,Hori(i),'liner','extrap'))/
5);
          SurLoc(2)=nsamp-
fix((interp1(ReefB_x,ReefB_z,Hori(i),'liner','extrap'))/5);
          SurLoc(3)=nsamp-
fix((interp1(Lamar6_x,Lamar6_z,Hori(i),'liner','extrap'))/5);
          SurLoc(4)=nsamp-
fix((interp1(Lamar4_x,Lamar4_z,Hori(i),'liner','extrap'))/5);
          SurLoc(5)=nsamp-
fix((interp1(Lamar2_x,Lamar2_z,Hori(i),'liner','extrap'))/5);
          SurLoc(6)=nsamp-
fix((interp1(Lamar2B_x,Lamar2B_z,Hori(i),'liner','extrap'))/5);
          SurLoc(7)=nsamp-
fix((interp1(SandB_x,SandB_z,Hori(i),'liner','extrap'))/5);
          SurLoc(8)=nsamp-
fix((interp1(Mck_x,Mck_z,Hori(i),'liner','extrap'))/5);

          for j=1:SurLoc(1)
                Z1(j,i)=11;
          end
          for j=SurLoc(1)+1:SurLoc(2)
                Z1(j,i)=Imp_Reef(i);
```

```matlab
        end
        for j=SurLoc(2)+1:SurLoc(3)
            Z1(j,i)=Imp_Lamar6(i);
        end
        for j=SurLoc(3)+1:SurLoc(4)
            Z1(j,i)=Imp_Lamar4(i);
        end
        for j=SurLoc(4)+1:SurLoc(5)
            Z1(j,i)=Imp_Lamar3(i);
        end
        for j=SurLoc(5)+1:SurLoc(6)
            Z1(j,i)=Imp_Lamar2(i);
        end
        for j=SurLoc(6)+1:SurLoc(7)
            Z1(j,i)=Imp_Unk(i);
        end
        for j=SurLoc(7)+1:SurLoc(8)
            Z1(j,i)=Imp_Mck(i);
        end
        for j=SurLoc(8)+1:nsamp
            Z1(j,i)=Imp_Mc(i);
        end
end

for i=79:106


        SurLoc=[0,0,0,0,0,0,0,0,0];
        SurLoc(1)=nsamp-
fix((interp1(PostLamar_x,PostLamar_z,Hori(i),'liner','extrap'))/
5);
        SurLoc(2)=nsamp-
fix((interp1(Lamar6_x,Lamar6_z,Hori(i),'liner','extrap'))/5);
        SurLoc(3)=nsamp-
fix((interp1(Lamar4_x,Lamar4_z,Hori(i),'liner','extrap'))/5);
        SurLoc(4)=nsamp-
fix((interp1(Lamar2_x,Lamar2_z,Hori(i),'liner','extrap'))/5);
        SurLoc(5)=nsamp-
fix((interp1(Lamar2B_x,Lamar2B_z,Hori(i),'liner','extrap'))/5);
        SurLoc(6)=nsamp-
fix((interp1(SandB_x,SandB_z,Hori(i),'liner','extrap'))/5);
        SurLoc(7)=nsamp-
fix((interp1(Mck_x,Mck_z,Hori(i),'liner','extrap'))/5);


        for j=1:SurLoc(1)
            Z1(j,i)=Imp_PostLamar(i);
        end
        for j=SurLoc(1)+1:SurLoc(2)
            Z1(j,i)=Imp_Lamar6(i);
        end
        for j=SurLoc(2)+1:SurLoc(3)
```

```matlab
        Z1(j,i)=Imp_Lamar4(i);
    end
    for j=SurLoc(3)+1:SurLoc(4)
        Z1(j,i)=Imp_Lamar3(i);
    end
    for j=SurLoc(4)+1:SurLoc(5)
        Z1(j,i)=Imp_Lamar2(i);
    end
    for j=SurLoc(5)+1:SurLoc(6)
        Z1(j,i)=Imp_Unk(i);
    end
    for j=SurLoc(6)+1:SurLoc(7)
        Z1(j,i)=Imp_Mck(i);
    end
    for j=SurLoc(7)+1:nsamp
        Z1(j,i)=Imp_Mc(i);
    end
end

for i=107:112


    SurLoc=[0,0,0,0,0,0,0,0,0,0];
    SurLoc(1)=nsamp-
fix((interp1(PostLamar_x,PostLamar_z,Hori(i),'liner','extrap'))/
5);
    SurLoc(2)=nsamp-
fix((interp1(Lamar6_x,Lamar6_z,Hori(i),'liner','extrap'))/5);
    SurLoc(3)=nsamp-
fix((interp1(Lamar5_x,Lamar5_z,Hori(i),'liner','extrap'))/5);
    SurLoc(4)=nsamp-
fix((interp1(Lamar4_x,Lamar4_z,Hori(i),'liner','extrap'))/5);
    SurLoc(5)=nsamp-
fix((interp1(Lamar2_x,Lamar2_z,Hori(i),'liner','extrap'))/5);
    SurLoc(6)=nsamp-
fix((interp1(Lamar3_x,Lamar3_z,Hori(i),'liner','extrap'))/5);
    SurLoc(7)=nsamp-
fix((interp1(Lamar2B_x,Lamar2B_z,Hori(i),'liner','extrap'))/5);
    SurLoc(8)=nsamp-
fix((interp1(SandC_x,SandC_z,Hori(i),'liner','extrap'))/5);
    SurLoc(9)=nsamp-
fix((interp1(SandB_x,SandB_z,Hori(i),'liner','extrap'))/5);
    SurLoc(10)=nsamp-
fix((interp1(Mck_x,Mck_z,Hori(i),'liner','extrap'))/5);

    for j=1:SurLoc(1)
        Z1(j,i)=Imp_PostLamar(i);
    end
    for j=SurLoc(1)+1:SurLoc(2)
        Z1(j,i)=Imp_Lamar6(i);
    end
    for j=SurLoc(2)+1:SurLoc(3)
```

```matlab
                Z1(j,i)=Imp_Lamar4(i);
        end
        for j=SurLoc(3)+1:SurLoc(4)
                Z1(j,i)=Imp_Lamar5(i);
        end
        for j=SurLoc(4)+1:SurLoc(5)
                Z1(j,i)=Imp_Lamar3(i);
        end
        for j=SurLoc(5)+1:SurLoc(6)
                Z1(j,i)=Imp_Lamar2(i);
        end
        for j=SurLoc(6)+1:SurLoc(7)
                Z1(j,i)=Imp_Lamar1(i);
        end
        for j=SurLoc(7)+1:SurLoc(8)
                Z1(j,i)=Imp_SandC(i);
        end
        for j=SurLoc(8)+1:SurLoc(9)
                Z1(j,i)=Imp_Unk(i);
        end
        for j=SurLoc(9)+1:SurLoc(10)
                Z1(j,i)=Imp_Mck(i);
        end
        for j=SurLoc(10)+1:nsamp
                Z1(j,i)=Imp_Mc(i);
        end

end

for i=113:120


        SurLoc=[0,0,0,0,0,0,0,0,0,0];
        SurLoc(1)=nsamp-
fix((interp1(PostLamar_x,PostLamar_z,Hori(i),'liner','extrap'))/
5);
        SurLoc(2)=nsamp-
fix((interp1(Lamar5_x,Lamar5_z,Hori(i),'liner','extrap'))/5);
        SurLoc(3)=nsamp-
fix((interp1(Lamar4_x,Lamar4_z,Hori(i),'liner','extrap'))/5);
        SurLoc(4)=nsamp-
fix((interp1(Lamar3_x,Lamar3_z,Hori(i),'liner','extrap'))/5);
        SurLoc(5)=nsamp-
fix((interp1(Lamar1_x,Lamar1_z,Hori(i),'liner','extrap'))/5);
        SurLoc(6)=nsamp-
fix((interp1(SandC_x,SandC_z,Hori(i),'liner','extrap'))/5);
        SurLoc(7)=nsamp-
fix((interp1(Unk_x,Unk_z,Hori(i),'liner','extrap'))/5);
        SurLoc(8)=nsamp-
fix((interp1(SandB_x,SandB_z,Hori(i),'liner','extrap'))/5);
        SurLoc(9)=nsamp-
fix((interp1(Mck_x,Mck_z,Hori(i),'liner','extrap'))/5);
```

```matlab
        for j=1:SurLoc(1)
            Z1(j,i)=Imp_PostLamar(i);
        end
        for j=SurLoc(1)+1:SurLoc(2)
            Z1(j,i)=Imp_Lamar6(i);
        end
        for j=SurLoc(2)+1:SurLoc(3)
            Z1(j,i)=Imp_Lamar5(i);
        end
        for j=SurLoc(3)+1:SurLoc(4)
            Z1(j,i)=Imp_Lamar3(i);
        end
        for j=SurLoc(4)+1:SurLoc(5)
            Z1(j,i)=Imp_Lamar1(i);
        end
        for j=SurLoc(5)+1:SurLoc(6)
            Z1(j,i)=Imp_SandC(i);
        end
        for j=SurLoc(6)+1:SurLoc(7)
            Z1(j,i)=Imp_Unk(i);
        end
        for j=SurLoc(7)+1:SurLoc(8)
            Z1(j,i)=Imp_SandB(i);
        end
        for j=SurLoc(8)+1:SurLoc(9)
            Z1(j,i)=Imp_Mck(i);
        end
        for j=SurLoc(9)+1:nsamp
            Z1(j,i)=Imp_Mc(i);
        end

end

for i=121:141


        SurLoc=[0,0,0,0,0,0,0,0,0,0];
        SurLoc(1)=nsamp-
fix((interp1(PostLamar_x,PostLamar_z,Hori(i),'liner','extrap'))/
5);
        SurLoc(2)=nsamp-
fix((interp1(Lamar5_x,Lamar5_z,Hori(i),'liner','extrap'))/5);
        SurLoc(3)=nsamp-
fix((interp1(Lamar4_x,Lamar4_z,Hori(i),'liner','extrap'))/5);
        SurLoc(4)=nsamp-
fix((interp1(Lamar3_x,Lamar3_z,Hori(i),'liner','extrap'))/5);
        SurLoc(5)=nsamp-
fix((interp1(Lamar1_x,Lamar1_z,Hori(i),'liner','extrap'))/5);
        SurLoc(6)=nsamp-
fix((interp1(SandC_x,SandC_z,Hori(i),'liner','extrap'))/5);
```

```matlab
        SurLoc(7)=nsamp-
fix((interp1(Unk_x,Unk_z,Hori(i),'liner','extrap'))/5);
        SurLoc(8)=nsamp-
fix((interp1(SandB_x,SandB_z,Hori(i),'liner','extrap'))/5);
        SurLoc(9)=nsamp-
fix((interp1(Mck_x,Mck_z,Hori(i),'liner','extrap'))/5);
        SurLoc(10)=nsamp-
fix((interp1(SandA_x,SandA_z,Hori(i),'liner','extrap'))/5);

        for j=1:SurLoc(1)
            Z1(j,i)=Imp_PostLamar(i);
        end
        for j=SurLoc(1)+1:SurLoc(2)
            Z1(j,i)=Imp_Lamar6(i);
        end
        for j=SurLoc(2)+1:SurLoc(3)
            Z1(j,i)=Imp_Lamar5(i);
        end
        for j=SurLoc(3)+1:SurLoc(4)
            Z1(j,i)=Imp_Lamar3(i);
        end
        for j=SurLoc(4)+1:SurLoc(5)
            Z1(j,i)=Imp_Lamar1(i);
        end
        for j=SurLoc(5)+1:SurLoc(6)
            Z1(j,i)=Imp_SandC(i);
        end
        for j=SurLoc(6)+1:SurLoc(7)
            Z1(j,i)=Imp_Unk(i);
        end
        for j=SurLoc(7)+1:SurLoc(8)
            Z1(j,i)=Imp_SandB(i);
        end
        for j=SurLoc(8)+1:SurLoc(9)
            Z1(j,i)=Imp_Mck(i);
        end
        for j=SurLoc(9)+1:SurLoc(10)
            Z1(j,i)=Imp_SandA(i);
        end
        for j=SurLoc(10)+1:nsamp
            Z1(j,i)=Imp_Mc(i);
        end

end

% Impedance Model plot
pcolor(Z1)
caxis([9,14])
set(gca,'ydir','reverse')
```

```
%Reflection Coefficient
for i=1:141
    for j=1:130
        RC_M1(j,i)=(Z1(j+1,i)-Z1(j,i))/(Z1(j+1,i)+Z1(j,i));
    end
end
```

wavelet generation

```
%Trapgen
% trapgen.m; by DRP; REVISED 30 JAN 2017
% This routine was modified from the trigen pass using
hp2
% Matlab routine for generating Ormsby time domain
trapezoidal bandpass wavelet
% with inputted lowcut, lowpass, highp2ass, and
highcut bandpass frequencies,
% as well as phase, and with ramped amplitude, showing
freq in both percent
% amplitude and power in dB, including phase in
radians, and stopping at the nyquist
% NOTE: there is NO duplication of amplitudes at
endpoints!
% NOTE: lc,lp1,lp2,hp1,hp2,and hc are the segment
endpoints

disp (' ')
disp ('DR Ps ORMSBY TIME-DOMAIN TRAPEZOIDAL BANDPASS
GENERATION MODULE')
disp (' ')
sr = 0.001;
nyq = (1/(2*sr));
ol = 0.5;
% note that this is effectively twice the operator
length in reality
t=-ol:sr:ol;
lc = 2;
lp1 =8;
hp2= 62.5;
%by subtracting one sr from hp2, this prohibits using
hp2 for two exact calculations
hc = 80;
phi =0;
```

```matlab
%or one could input the phaseangle in degrees as above
where
phi = phi*pi;
%implicitly includes pi in the radians
%phi = phaseangle*180/pi and
%phi is the phase in radians
%these next two lines are more explanatory than
concise as they
%represent the increments
lp2 = lp1 + (sr/(hp2-lp1))*(hp2-lp1);
hp21 = hp2 - (sr/(hp2-lp1))*(hp2-lp1);
%sets endpoints that will not be duplicated at lp and
hp2
alc = 0;
alp = 1;
alp1 = alp;
ahp2 = 1;
ahc = 0;
%a.. indicate amplitudes for incremental frequencies
x1 =1;
x2 = 1;
x3 = 1;
% these x values are initial settings required for the
next lines
mf1 = (lp1-lc)/(max(x1));
mf2 = (hp2-lp2)/(max(x2));
bf2 = lp2;
% f represents frequencies for slopes and intercepts
ba2 = alp1;
ahp2 = (ahp2-alp1)/(max(x2))*(1-sr) + ba2;
alp2 = (ahp2-alp1)/(max(x2))*sr + ba2;
ma2 = (ahp2-alp2)/(max(x2));
ma3 = (ahc-ahp2)/(max(x3));
mf3 = (hc-hp2)/(max(x3));
bf1 = lc;
ba1 = alc;
bf3 = hp2;
ba3 = ahp2;
ma1 = (alp1-alc)/(max(x1));

incr1 = sr/(lp1-lc);
incr2 = sr/(hp21-lp2);
incr3 = sr/(hc-hp2);
```

```
y1 =0;
y2 = 0;
y3= 0;
%these y's are initial settings for the following
loops

            for x1 = 0:incr1:1
                y1 = y1 +
((x1*ma1)+ba1).*cos(2*pi*((x1*mf1)+bf1)*t + phi);
            end

            for x2 = 0:incr2:1
                y2 = y2 +
((x2*ma2)+ba2).*cos(2*pi*((x2*mf2)+bf2)*t+phi);
            end

            for x3 = 0:incr3:1
                y3 = y3 +
((x3*ma3)+ba3).*cos(2*pi*((x3*mf3)+bf3)*t + phi);
            end


y = y1 + y2 + y3;
F = length (y);
y = y/(F);
% normalizes the amplitudes which accumulate for
% the amplitude plots by dividing
% by the number of discrete summed functions
% ytrap = y;
ytrap = y;
%temporarially saves ytrap for later use
Y = fft(y);
%Ytrap = Y;
%n=length (Y);
%power = abs (Y(1:n/2)).^2;
%freq = (1:n/2)/(n/2)*nyq;
ctr=0;
N = length(t);
Ntrap = N;
k = 0:(N-1);
ampY = Y.*conj(Y);
%obtains the real amplitudes
ampY = sqrt(ampY);
%converts power back to amplitude
```

```matlab
fracampY = ampY/ (max(ampY));
percentampY = fracampY * 100;
hertz = k*(1/(N*sr));
fracampy = y/(max(y));
%normalizes amplitude to 100% for plotting
subplot (2,2,1), plot (fracampy,-t,ctr,-t)
ylabel('Time(sec)'), title('Band pass of 2 8 80 125')
axis ([-2 2 -1 1])
g = unwrap (angle (Y));
%unwrap is an equivalent phase command
%which eliminates the 180 degree jumps
subplot(2,2,2), plot (hertz, g)
%axis ([0 nyq -360 360])
%ylabel ('Degrees'), title ('PHASE')
axis ([0 nyq -5 5])
ylabel ('Pi Radians'), title ('PHASE')
subplot(2,2,3), area (hertz, percentampY)
%subplot (2,2,3), area (hertz, ampY)
axis ([0 nyq 0 200])
ylabel ('Per Cent'), xlabel ('Hertz'), title
('AMPLITUDE')
subplot (2,2,4), area (hertz, 10*log10(abs(ampY.^2)))
title ('POWER')
axis ([0 nyq 0 100])
ylabel ('dB'), xlabel ('Hertz')
figure %allows the additional figure page to be
printed
plot (fracampy,-t,ctr,-t)
ylabel('Time(sec)'), title('Band pass of 2 8 62.5 80')
axis ([-2 2 -1 1])
```

Synthetic traces generation

```matlab
%SynGen
% syngen; created by Dr. P. REVISED 30 JAN 2017.
% usese subroutine for convolving two previously
generated signals
% demonstrating frequency in amplitude, but stopping
at the nyquist
% NOTE THAT FIRST SIGNAL SETS PRIORITY FOR STARTING
TIME!

disp (' ')
disp ('SYNTHETIC GENERATION MODULE')
```

```matlab
disp ('MUST HAVE PREVIOUSLY GENERATED A RC SERIES,
e.g. yrc, AND A FILTER, e.g. ytrap')
disp ('AT SIMILAR SAMPLE RATES.')
disp (' ')
sig1 = RC_M2;
sig2 = ytrap;
sr = 0.001;
nyq = 1/(2*sr);
N1 = length (sig1(:,1));
N2 = length (sig2);
t1 = 0:(N1-1);
t2 = 0:(N2-1);
%allows input signals to generate t functions of
correct lengths
%sig1 = sig1./max(abs(sig1));
%sig2 = sig2/max(abs(sig2));
sig1(isnan(sig1)) = 0;
for i=1:141
%normalizes the two signal amplitudes (11/08/99)
yraw1(:,i) = conv (sig1(:,i), sig2);
N3 = length (yraw1(:,i));
%QUESTION: NEED TO FIX THE SHIFT OF THE TIME AFTER
CONVOLUTION:
midyraw = (N3 + 1)/2;
%midyraw = (N3)/2;
midsig1 = (N1 + 1)/2;
%midsig1 = (N1)/2;
Lindex = midyraw - midsig1 + 1;
%%Lindex = midyraw - midsig1 -2 ;
Hindex = midyraw + midsig1 - 1;
%%Hindex = midyraw + midsig1 - 2;
%y(:,i) = yraw(Lindex:Hindex,i);
yraw1(:,i) = yraw1(:,i)./(max(abs(yraw1(:,i))));
fracnoise =0.05;
noise = fracnoise*randn(size(yraw1(:,i)));
%adds user input of noise
%yraw1(:,i) = yraw1(:,i) + noise;
end
ysyn = yraw1(Lindex:Hindex,:);
%temporarially saves y for later use
Y= fft (ysyn);
ctr=0;
%freq = (1:n/2)/(n/2)*nyq;
      N = (N1);
```

```matlab
        %t = 0:sr:((Nsum-2)/100);
        %t = 0:sr:(Nsum);
        t = 0:(N1-1);
        k = 0:(N1-1);
        ampY = Y.*conj(Y);
ampY = sqrt(ampY);
%converts power back to amplitude
fracampY = ampY./ (max(ampY));
percentampY = fracampY * (100);
hertz = k*(1/(N*sr));
%fracampy = y/(max(y));
subplot (2,2,1), plot (sig1,-t1,ctr,-t1)
ylabel('Time (ms)'), title('REFLECTIVITY')
%axis ([-2 2 -1 0])
%g = unwrap (angle(Y));
subplot(2,2,2), plot (sig2, -t2, ctr, -t2)
%axis ([0 nyq -360 360])
%ylabel ('Degrees'), title ('PHASE')
%axis ([0 nyq -5 5])
ylabel ('Time (ms)'), title ('INPUT WAVLET')
%%subplot (2,2,3), plot (y, -t, ctr, -t)
subplot (2,2,3), plot (ysyn, -t, ctr, -t)
ylabel ('Time (ms)'), title ('SYNTHETIC')
%%axis ([-2 2 -length(y) 0])
%subplot(2,2,4), area (hertz, percentampY)
axis ([0 nyq 0 100])
ylabel ('Per Cent'), xlabel ('Hertz'), title
('SYNTHETIC AMP.SPEC.')

for i=1:141
    ysyn_tran1(:,i)=ysyn(:,i)+i;
end
plot (ysyn_tran1, -t, ctr, -t,'b')
```